Raman investigations of In(Ga,Al)As/InP layers

Boom, H.

Award date:
1996

Technische Universiteit Eindhoven
Faculteit der Technische Natuurkunde
Vakgroep Vaste Stof Fysica

Raman Investigations of In(Ga,Al)As / InP Layers

Herman Boom
Oktober 1996

Report of a graduation project at the Solid State division of the Faculty of Applied Physics at the Technical University Eindhoven.

afstudeerdocent	: Dr. ir. F.A.P. Blom
begeleider TUE	: Ir. C.M. van Es
adviseur RWTH Aachen / Universität Würzburg	: Prof. dr. J. Geurts

Summary

The In(Ga or Al)As / InP system enjoys a rapidly increasing interest for application in opto-electronic devices. Generally, the layer structures in these devices are grown with high-tech epitaxial techniques like Molecular Beam Epitaxy (MBE) and Chemical Beam Epitaxy (CBE).

In this work we investigate bulk InAlAs layers grown by MBE, as well as InAs / InP and InGaAs / InP superlattices grown by CBE. As a basis for these layer structures we used InP substrates. The MBE samples were grown in order to optimise the growth of lattice matched ternary material, by changing the annealing time during which the substrate is cleaned before the growth. The CBE samples were grown to optimise the growth of InGaAs / InP superlattices, i.e. obtain a good surface morphology (low defect density and no macroscopic steps). Therefore, the CBE samples are grown on various misorientations, which gives rise to different growth mechanisms, as well as with different growth interrupt sequences (GIS), which allow control over the interface layers.

Non-resonant Raman measurements (inelastic light scattering) have been performed on MBE samples in order to obtain additional information on the interface layer between the bulk InAlAs layer and the substrate. From photoluminescence measurements we know that this interface layer has a complex 3D structure [13]. However, apart from a weak structure around 246 cm^{-1} which we associate with strained InAs at the interface, no additional information could be obtained from the spectra.

On the CBE samples we also performed Raman measurements. In the spectra of the samples consisting of the InAs / InP superlattices no intensity could be found in the As-region of the spectrum. Further, two additional peaks are observed at 305 cm^{-1} and 310 cm^{-1}. These peaks are assigned to an interface phonon and the InP transverse optical phonon. However, unambiguous identification is not possible.

Differences in the spectra of the InGaAs / InP superlattices grown on various substrate misorientations and with different GIS, were hardly observed. Thus little or no additional information is obtained from these spectra. However, a broadening in the spectral region between 265 cm^{-1} and 270 cm^{-1} is observed for all these samples. In our opinion this can be due to an indium gradient somewhere in the InGaAs layers.

Generally, we conclude that Raman spectroscopy is unsuited for giving additional information on the small and subtle differences between the different samples. Nevertheless, Raman spectroscopy could be a very powerful instrument for interface and layer characterisation, especially when resonant Raman measurements are possible.

Contents

Technology Assessment

The increasing use of telecommunication networks due to recent developments like video-on-demand and the explosive growth of internet-users, requires a larger bandwidth which is offered by optical connections instead of electrical ones. Therefore, optical devices are necessary that operate at wavelengths near the dispersion minimum of silica fibres (1.3 μm) or near the minimum of fibre loss (1.55 μm). In this work we study the material systems on the basis of III/V semiconductor material, which are of interest for the realisation of such devices, namely the In(Al or Ga)As on InP system. Samples belonging to these material systems have been grown with Molecular Beam Epitaxy (MBE) and Chemical Beam Epitaxy (CBE).

In order to optimise the MBE growth of InAlAs, bulk InAlAs has been grown under various growth conditions. A complication which arises in these samples is the formation of InAs interface layers due to substitution of P-atoms by As-atoms. These interface layers are a main subject in this work. The optimisation of the CBE growth involves the search for a substrate misorientation that gives a good surface morphology, i.e. a low defect density and no macroscopic steps. Further, in CBE samples, interfaces are formed with different growth interrupt sequences (GIS). The influence of the substrate misorientation and the GIS on the interface layers is another part of this work.

In this work we use Raman spectroscopy to obtain additional information on the interfaces. Raman spectroscopy is especially interesting, because of the sensitivity for individual layers/material through the strain and/or composition induced shift of their characteristic phonon frequencies.

After a brief introduction on III/V semiconductors and some aspects related with them (chapter 1), an overview of MBE and CBE growth is given (chapter 2). In chapter 3 we consider the lattice dynamics of (cubic) crystals, after which we describe the Raman effect and Raman spectroscopy (chapter 4), and the experimental set-up (chapter 5). The results of this study are presented in chapter 6 and completed with the conclusions in chapter 7. Finally, we give some suggestions for further research (chapter 8).

1. III/V Semiconductors

The III/V semiconductors are of great importance in today's semiconductor physics and device technology. They are an alternative for the elementary semiconductors germanium (Ge) and sillicium (Si). For both these materials the semiconductor technology has reached its limitations in many ways, especially in applications for optical devices where the indirect bandgap is a great disadvantage. The III/V materials have a direct bandgap, resulting in much better optical performance. Further, III/V materials have a larger electron mobility compared to Si and Ge. These two properties make III/V semiconductors very interesting for application in opto-electronic devices. Moreover, with III/V semiconductors we are not restricted to the 'pure' materials, like GaAs, AlAs and InAs, but are also able to use ternary compounds, like $In_{1-x}Ga_xAs$ and $Al_{1-x}Ga_xAs$, or even quartenary compounds. This offers great opportunities for bandgap engineering, since the bandgap for such compounds depends on the composition. Also other effects like strain, give additional instruments to manipulate the bandgap.

Probably the most developed structures are based on the material system $GaAs/Al_{1-x}Ga_xAs$. However, they can not be used in the field of optical telecommunication because the bandgap is too large, resulting in optical transitions with wavelengths in the visible range (500 - 800 nm) instead of in the required infra-red (IR) range (1,3 to 1,55 μm). Therefore, the material system $In_{1-x}(Ga,Al)_xAs_yP_{1-y}$ / InP enjoys a rapidly increasing interest during the last few years. It offers the advantages described above for III/V compounds and has the appropriate energy transitions, making the material system interesting for application in high-frequency devices and opto-electronic devices for telecommunication. However, the fabrication of structures of these materials is much more sophisticated compared to the fabrication of structures containing the elementary semiconductors.

In this chapter we discuss some basic aspects of III/V semiconductors. We start with the description of the lattice structure in section 1.1. Next we focus on the consequences of their use in layer structures, treating concepts like strain and critical layer thickness (section 1.2).

1.1 Lattice Structure

Most of the III/V semiconductors have a zinc-blende structure. More accurately: they all have a lattice with a $\bar{4}3m$ symmetry point group (international notation), also known as T_d-symmetry in the still often used Schönfliess notation.

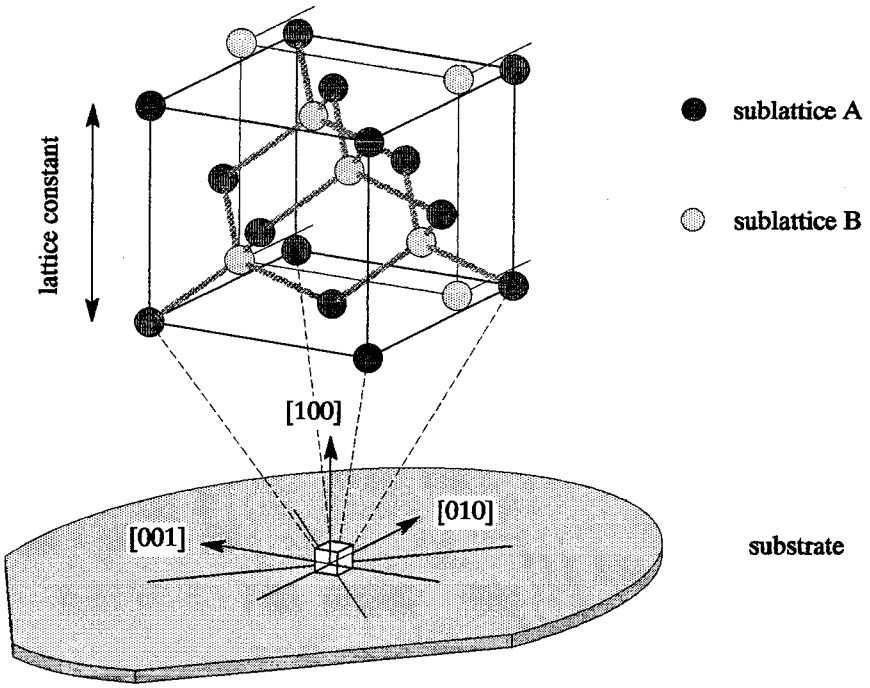

Figure 1.1: The two sublattices forming the lattice of a general III/V compound and the crystallographic directions (indicated by arrows) with respect to the substrate.

The zinc-blende structure consists of two face-centered-cubic (fcc) sublattices, where one sublattice is translated by ¼ of a body diagonal with respect to the other sublattice. The primitive cell of the lattice contains two atoms, one group III atom and one group V atom. The total lattice formed by the two sublattices is shown in Figure 1.1, together with the crystallographic directions and the orientation of the crystal lattice with respect to a substrate (see also section 2.3). On these substrates the layer structures are epitaxially grown. On one sublattice all group III elements are positioned, while at the other sublattice only group V elements are placed. As a result each atom of one group is tetraedically surrounded by atoms from the other group. Note that when we look down on a substrate (in the [-100] direction), only one group of atoms, III or V, occupies the top surface. This implies that a layer consists of periodic group III and group V atomic layers.

1.2 III/V Ternary Compounds: Strain

The combination of two binary materials AC and BC, yields a ternary compound $A_{1-x}B_xC$, where x represents the composition. We assume that the atoms A and B are randomly distributed over their sublattice, i.e. there is no alloy clustering. The properties of the compound, like lattice constant and bandgap, depend on the composition. We can find the lattice constant of the ternary compound by linear interpolation between the binary values via the composition. This is called Vegard's law. Although, it is often accurately used for the lattice constant, we must be very careful to use it for other properties like the bandgap, because non-linear effects may play an important role. Nevertheless, in first approximation the dependence is linear. Applying Vegard's law for the lattice constant of the ternary $A_{1-x}B_xC$, results:

$$a_{ABC} = a_{AB} \cdot x + a_{AC} \cdot (1-x) \qquad (1.1)$$

where a_{AC} and a_{BC} are the lattice constants of material AC and BC respectively. Later we will use this law to obtain the phonon frequencies of ternary compounds (section 3.4).

Today, ternary compounds are quite generally used in the growth of semiconductor layer structures. These layer structures are epitaxially grown on a substrate of semiconductor material. In other words, the substrate and the layers form a mono-crystalline structure. When the lattice constant of the material of the layer does not match that of the substrate, mono-crystalline growth is still possible by accommodation of the in-plane lattice constant, which means that shear strain is introduced in the layer. The lattice constant in the plane (100) perpendicular to the growth direction is, however, uniform for the entire structure. This implies that the unit cell of the lattice of the layer is forced into an adapted shape. The volume of the unit cell must re-

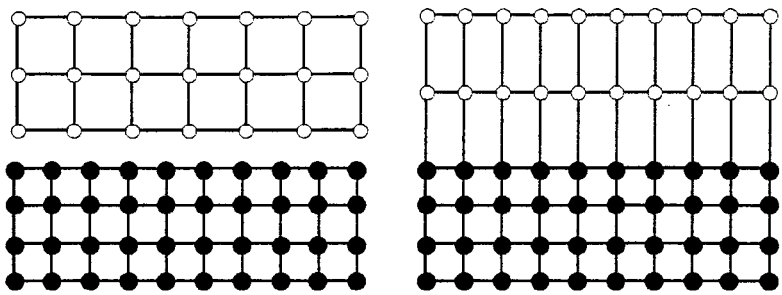

Figure 1.2: A strain induced tetragonal distortion of the unit cell due to a lattice mismatch. On the right side the layer is in compression.

main constant, since the hydrostatic pressure or strain does not change [1]. A lattice deformation under this condition is called a tetragonal distortion. The shortening of the lattice constant in the (100) plane (in plane) then results a lengthening of the lattice constant in the [100] direction, and vice versa. This is shown in Figure 1.2, where the difference in lattice constant is exaggerated for the sake of clarity. Strain due to a lattice constant of the layer larger than that of the substrate is called compression, while strain induced by a smaller lattice constant of the layer is called tension.

A measure for the strain is the relaxed mismatch , given by:

$$\frac{\Delta a}{a} = \frac{a_L - a_S}{a_S} \qquad (1.2)$$

where a_L represents the in plane lattice constant of the layer in absence of strain, and a_S is the lattice constant of the substrate. Normally the mismatch is expressed in percent or ppm. The mismatch of InAs to InP is about 3 percent, which is extremely large.

In order to grow a layer of a ternary compound without strain the lattice constant of one constituent binary compound must be larger and the other must be smaller than the lattice constant of the substrate. Then there exists a composition of the layer which yields a lattice constant similar to that of the substrate. A layer with such a composition can be grown on the substrate without resulting strain. In that case the layer is said to be lattice matched. The lattice matched compositions for $In_{1-x}Ga_xAs$ and $In_{1-x}Al_xAs$ on a InP substrate are x = 0.477 and x = 0.468 respectively.

During growth of a strained layer on a substrate, the lattice constant of the layer will start to relax to its unstrained value at a critical thickness d_c. This process is accompanied by the creation of misfit dislocations, which deteriorate the crystallographic quality of the structure. For the relation between the lattice mismatch (or strain) and the critical thickness various models exist. The most commonly used is given by Matthews and Blakeslee [2]:

$$d_c = \frac{b}{4\pi\varepsilon_{max}} \cdot \frac{(1 - \upsilon \cos^2 \alpha)}{(1 + \upsilon) \cdot \cos\lambda} \cdot (\ln\frac{d_c}{b} + 1) \qquad (1.3)$$

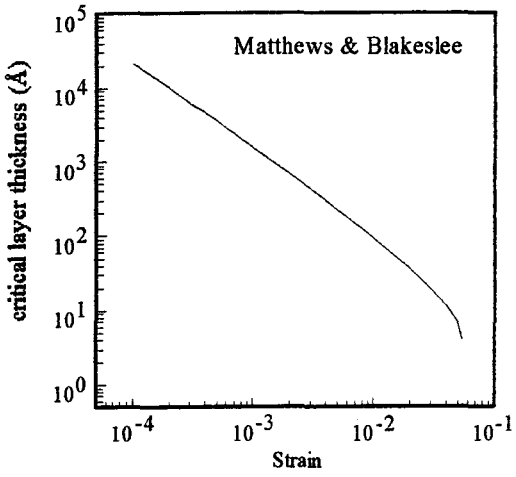

Figure 1.3: Relation between critical thickness and strain according to Matthews and Blakeslee [2].

where b is the length of the Burger's vector giving the translation of the lattice due to the misfit dislocation. Further, α is the angle between the Burgers vector and the dislocation line, λ is the angle between the slip directions, ε_{max} is the maximum strain for a layer with critical thickness d_c, and υ is Poisson's ratio. Relation (1.3) is depicted in Figure 1.3. Clearly, the critical thickness decreases steeply for increasing strain. This gives limitations on the amount of strain which can be incorporated. Nevertheless, in thinner layers a significant amount of strain can be incorporated without giving rise to relaxation. It is possible to accomplish strain compensation for thick layers. This is done by growing thin heavily opposite strained layers between the otherwise relaxed layers [3]. Generally, a layer is said to be pseudomorphic when no relaxation is present.

Despite limitations such as the critical thickness, strain offers important possibilities for bandgap engineering. For instance, the degeneration of the light-hole and heavy-hole valence bands is lifted due to shear strain. The conduction band is also influenced by shear strain, but in a far less extent. The influence of strain on the electronic band structure of a semiconductor is described by C.G. van de Walle, based on electronic deformation potentials and the model solid theory [1].

A practical convenient method to determine the mismatch, is X-ray diffraction (XRD). This method is very sensitive for variations in the lattice constant and thus for compositions of pseudomorphic layers. For a detailed description of XRD techniques we refer to [4]. It was XRD examinations that gave rise to further investigation of the interface layers, which is one of the main subjects in this work. Before we can look into them we need a deeper understanding of the growth, epitaxial techniques and the effects that give rise to interface layers. All this will be discussed in the next chapter.

2. Epitaxial Growth

In this chapter we discuss the epitaxial growth. The samples investigated in this work are grown with Molecular Beam Epitaxy (MBE) or with Chemical Beam Epitaxy (CBE). We start with an introduction on the basics of the growth-process and a description of the MBE and CBE system (section 2.1). After that, in section 2.2 interface layers and their formation in MBE- and CBE-growth are described. Next, we discuss the substrates and the associated growth mechanisms (section 2.3). Finally, the different structures of the samples investigated in this work are given in section 2.4.

2.1 Epitaxial Techniques

Molecular Beam Epitaxy

Molecular Beam Epitaxy (MBE) is an epitaxial growth process that involves the reaction of one or more thermal beams of atoms and molecules of the constituent elements with a crystalline surface held at a suitable temperature under ultra-high-vacuum (UHV) conditions. This UHV is achieved with an ion-getter-pump, a titanium sublimation pump and a cryo-pump. Additionally, the growth chamber contains liquid nitrogen cooled shrouds, which 'adsorb' most of the background gas molecules/atoms and thus allow a better evacuation of the growth chamber to a basic pressure of 10^{-10} mbar. In Figure 2.1 an overview of the MBE system is shown. The effusion cells generate molecular beams by evaporation of elemental source material. Accurate control of the cell temperature is required to obtain a constant flux of material. Each source or effusion cell has its own externally controlled shutter. These shutters permit rapid interruption of the beam species, which allows us to change abruptly the composition of the epitaxial layer. Abrupt interfaces on the scale of one monolayer (ML) can be achieved. The film grows on a substrate which is mounted on a molybdenum substrate holder. This holder rotates in order to achieve highly uniform epitaxial layers. The distance between the effusion cells and the substrate is about 35 cm. The substrate is heated to the growth temperature by resistive heating. A load-lock attached to the entrance of the growth chamber allows the exchange of substrates while maintaining the UHV.

In-situ characterisation is possible due to the UHV conditions. In order to monitor the surface structure, the MBE is equipped with a reflective-high-energy-electron-diffraction (RHEED) gun with a fluorescent screen. A re-

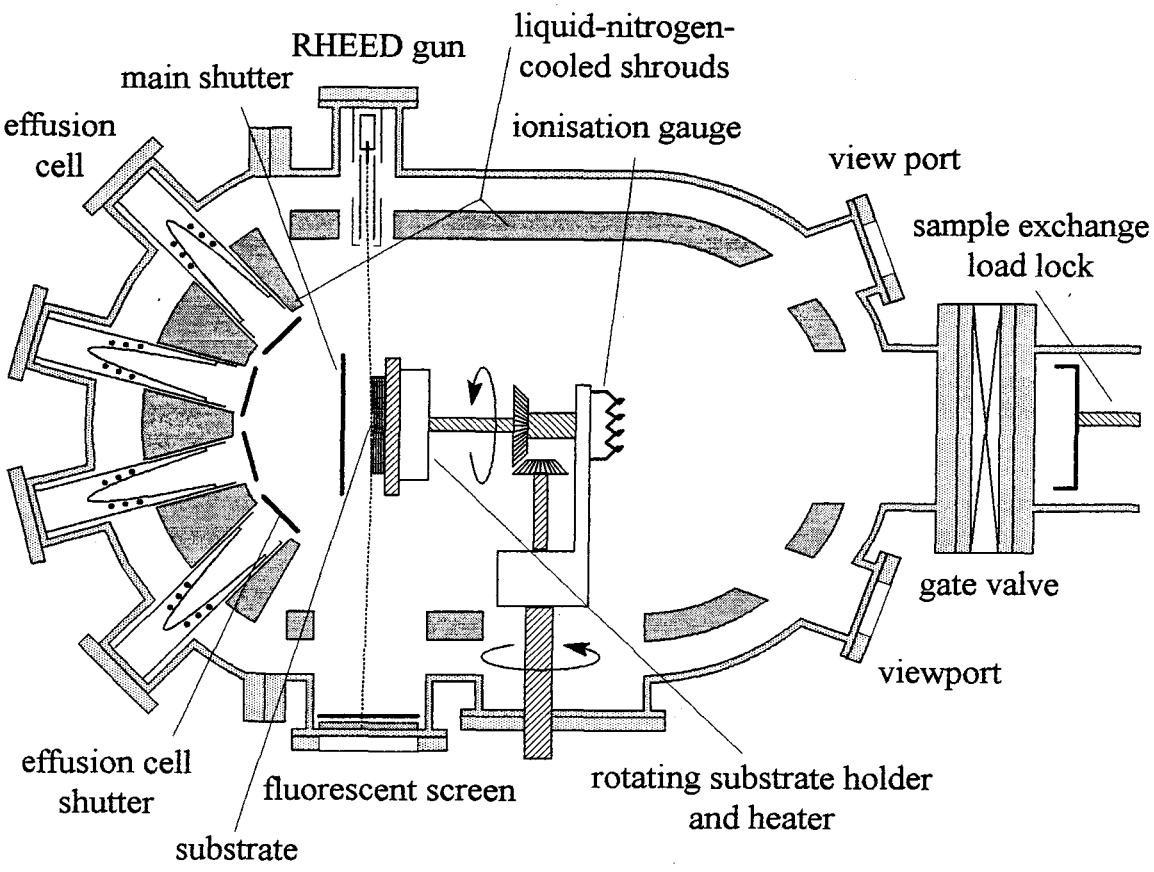

Figure 2.1: Overview of the MBE growth chamber. The different components and their function are described and explained in the text.

sidual gas analyser or mass spectrometer is present to determine the background gases in the system.

At the heated crystalline surface, epitaxial growth of III/V compounds involves a series of subsequent events. First the adsorption of the constituent atoms and molecules, next the dissociation of the adsorbed molecules and the surface migration and finally the incorporation of the atoms in the crystal lattice, resulting in nucleation and growth.

The available materials in the MBE are: elemental aluminium (Al), gallium (Ga), indium (In) and arsenic (As). Note that there is no phosphorus available. This is due to the fact that it is difficult to obtain a stable flux of evaporating elemental phosphorus.

Chemical Beam Epitaxy:
We will now discuss briefly the process Chemical Beam Epitaxy (CBE). This technique combines the UHV technology of MBE with the gaseous starting materials of Metal Organic Vapour Phase Epitaxy (MOVPE) and therefore allows the growth of phosphorus containing material.

A basic overview of the CBE system is shown in Figure 2.2. The source materials are Tri-Methyl-Indium $In(CH_3)_3$ (TMIn), Tri-Ehthyl-Gallium $Ga(C_2H_5)_3$ (TEGa), arsine AsH_3 and phosphine PH_3. The group III and the group V source materials are passed through separate injectors into the UHV growth chamber, where they form two molecular beams. The group V precursors (hydrides) are pre-cracked in a high temperature injector (at a temperature of 850 °C). The low temperature injector of the metalorganics is kept at a temperature of 60 °C to avoid condensation of these materials. Their decomposition occurs on the heated substrate, which is mounted on a rotating substrate holder, on order to achieve highly uniform layers.

All gas flow rates are regulated by mass flow controllers (MFC). A run/vent procedure is used for gas switching. Depending on the position of the run/vent valve, the gas flow is directed into a run line to the injector and subsequently the growth chamber, or into a vent line. In this way, gas flow transients due to pressure build-up are prevented. The superfluous gases from the vent line and the growth chamber are pumped to a scrubber, which filters out the poisonous components.

The UHV (10^{-10} mbar) in the growth chamber is achieved by means of a turbo molecular pump and liquid nitrogen cooled shrouds. A loadlock attached to the growth chamber permits exchange of substrates without breaking the UHV conditions.

The growth of the epitaxial film on the substrate with CBE involves a series of events. First, the molecules from the molecular beams are adsorbed at the crystalline surface. After that, the metalorganic molecules and the group V molecules (As_2 and P_2) thermally dissociate into atoms and finally are incorporated in the layer. During growth surface analysis is possible with RHEED, while the partial pressure of the constituent elements can be measured with a mass spectrometer positioned behind the substrate holder.

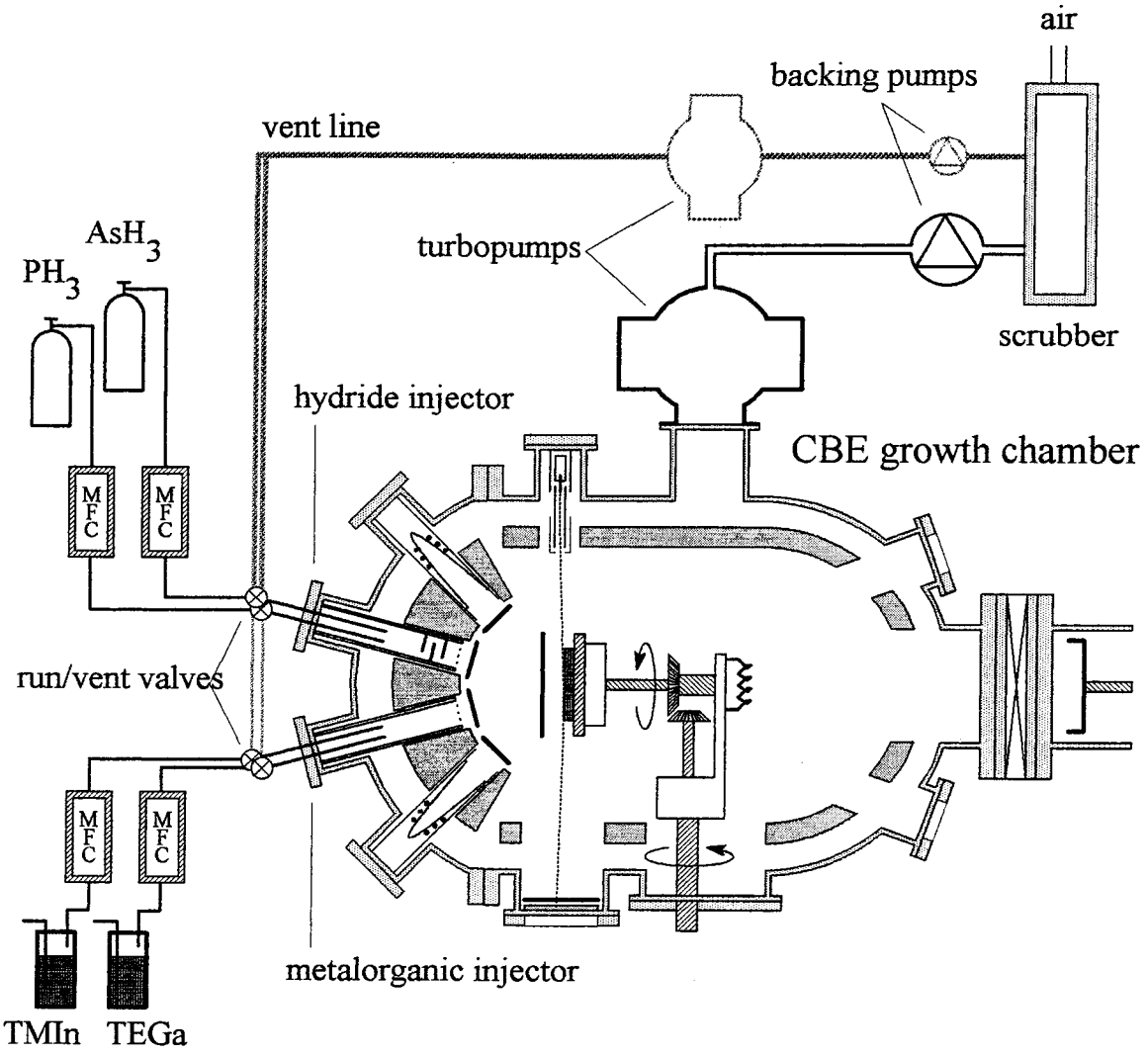

Figure 2.2: Basic overview of the CBE growth chamber and gas manifold. The different components and their functions are explained in the text.

2.2 Interface Layers

In this section we discuss the interface layers. These are layers which are in principle not intentionally grown and arise at the boundaries of two adjacent layers. The interface layers can be either intrinsic or formed by rearranging processes. They can also be intentionally grown. Generally, interface layers differ from the neighbouring layers by composition, thus forming an additional layer in the structure.

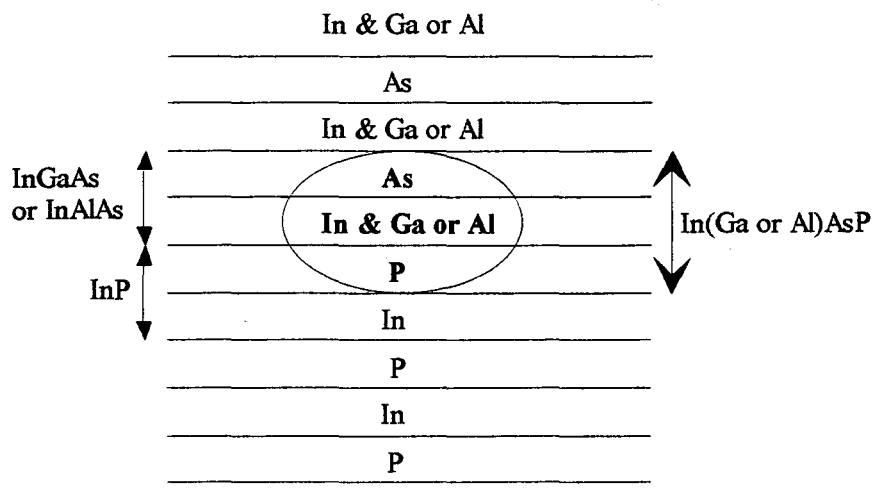

Figure 2.3: The intrinsic (quartenary) interface layer $In_{1-x}(Ga \text{ or } Al)_xAs_{1-y}P_y$ at the $InP/In_{1-x}(Al \text{ or } Ga)_xAs$ interface.

First we consider the intrinsic interfaces, which are always present due to the transition of one material to the other. For instance, look at the transition from InP to a ternary layer $In_{1-x}Al_xAs$ or $In_{1-x}Ga_xAs$, as shown in Figure 2.3. Obviously, when considering the sequence of atomic layers near the material transition (indicated with the small arrows in Figure 2.3), the presence of an interface layer with deviating composition is not clear. Yet starting from the point of view that the bonds of the group III atom layers to the group V atom layers matter, instead of the atomic layers, an $In_{1-x}Ga_xAs_yP_{1-y}$ and $In_{1-x}Al_xAs_yP_{1-y}$ interface for $In_{1-x}Ga_xAs$ and $In_{1-x}Al_xAs$ on InP respectively is concluded. This is indicated in Figure 2.3 with a ellipse.

We now consider explicitly the intrinsic interface layer of a bulk $In_{1-x}Ga_xAs/In_{1-x}Al_xAs$ layer, grown by MBE, on InP substrates. The substrates are epi-ready, meaning that there is an oxide-layer on top of it, which protects the substrate against impurities and environmental influences (oxygen). During its mounting on the holder, the substrate is exposed to the atmosphere, which leads to the adsorption of H_2O at the surface. Before the growth can begin, we have to remove both H_2O and the oxide-layer from the substrate. This is achieved with an annealing procedure as shown in Figure 2.4. First, the wafer is placed into the entry/exit chamber, in which it is heated to a temperature of about 200 °C. At this temperature the H_2O is desorbed from the substrate surface. Then the substrate is transported to the buffer chamber, after which it is placed in the growth chamber where the oxide-layer is removed. This is achieved by heating the substrate to a temperature above the growth temperature (thus more than 480 °C), at which it is kept for the annealing time t_{anneal}, typically in the order of minutes. However, at tempera-

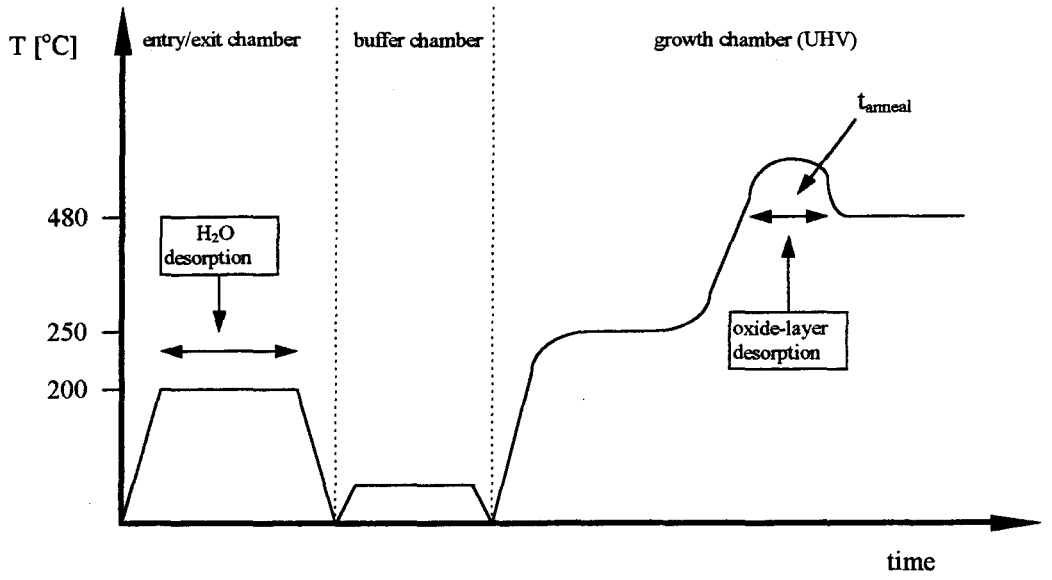

Figure 2.4: Annealing procedure for an InP substrate in order to evaporate the water out of the substrate and to remove the oxide-layer. The entire procedure is explained in the text.

tures higher than 360 °C, incongruent evaporation InP gives rise to sublimation of phosphorus and thereby the formation of indium droplets. This results in degradation of the crystalline InP surface. Hence the substrate is no longer suited for epitaxial growth. To compensate for the P-atoms evaporating from the surface, we would like to offer phosphorus to the surface. In the MBE system, however, there is no phosphorus available and we have to use arsenic species instead. At least this implies that the upper layer of P-atoms is then substituted by As-atoms, which means that the intrinsic interface as depicted in Figure 2.3 is shifted by 1 ML. However, from literature it is known that the layer between the InP substrate and layer is 6 ± 1 Å or 2 ML thick and consists of InAs [6,7]. This result for MBE was later confirmed for other epitaxial techniques, like CBE [3] and MOVPE [8], which indicates that the substitution process for these epitaxial techniques is similar. We describe the substitution process by a two-fold process, as suggested in reference [9]. During the first stage the top monolayer of the phosphorus is substituted (1 sec. for CBE). The second stage involves the substitution of the second layer of P-atoms. This process, however, is much slower (approximately 10 sec. for CBE).

Simultaneously with the substitution process another effect arises, namely the formation of InAs islands. This is the transition from a 2D to 3D formation of interface layers. The process is assumed only to involve the upper monolayer InAs. Due to the extremely heavy compressive strain it is ener-

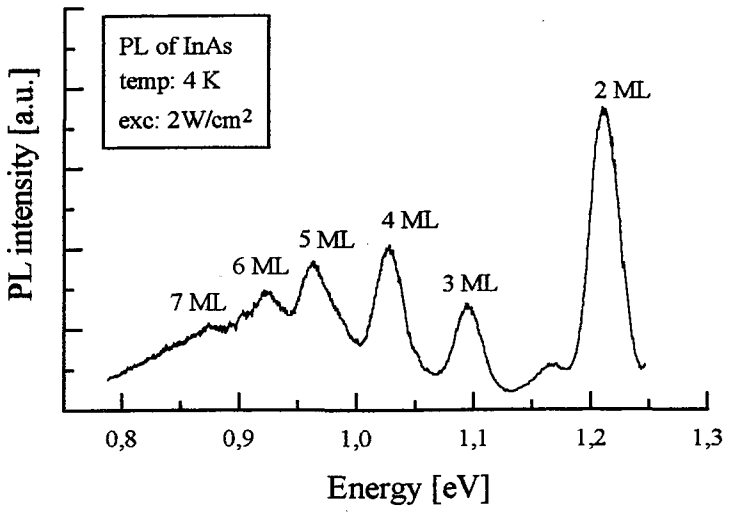

Figure 2.5: Photoluminescence spectrum at 4 K of the InAs islands in a MBE sample.

getically profitable for the layer to minimise the surface-volume ratio, which leads to elastic relaxation and the formation of InAs islands. Recent studies show that the strain is mainly localised at the edges of such islands. Due to the difference in band-edge, we have an extra possibility to proof the existence of the interface layer, namely with photoluminescence (PL) [10]. In Figure 2.5 the photoluminescence spectrum of a MBE sample is shown. Each peak represents an InAs island with a discrete thickness in ML. The large broadness of these peaks is assumed to be due to the various lateral dimensions of the islands and the roughness on top of them, which both give rise to a partial exclusion of the exciton. Note that the islands have a thickness up to 7 ML, while the initial InAs layer is about 2 ML. Gustafsson was one of the first who examined the island formation [11]. He used spatially resolved cathode-luminescence. According to his study the islands have lateral diameters in the range of 10-50 nm. Recently, the formation of interface layers and InAs islands, due to the annealing process, was thoroughly investigated in [12]. In that study, spectra similar to that in Figure 2.5 are presented. The influence of the annealing time, during the heating of the InP substrate to the growth temperature, on the island formation is discussed in [13]. From this study it becomes clear that we can only marginally influence the P by As substitution and subsequent the formation of InAs islands.

In CBE there is no substitution as phosphorus is available. However, it is still possible to expose an InP surface to As species and thus substitute P by As atoms. The substitution process under CBE can be better controlled, as the exposure time can be scaled down to the order of seconds. Consider the

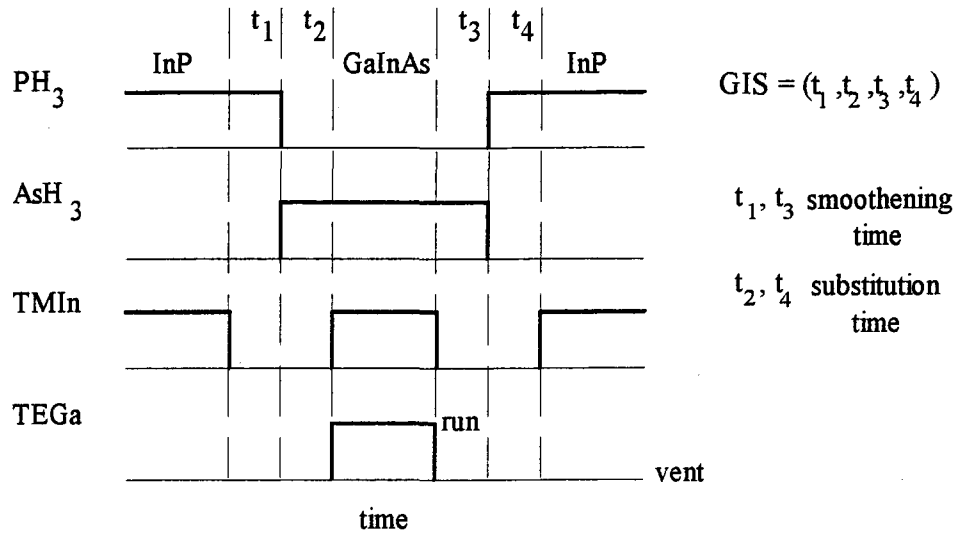

Figure 2.6: Growth-Interrupt-Sequence (GIS) for an $In_{1-x}Ga_xAs/InP$ superlattice. The different times and symbols are explained in the text.

growth of an InP / $In_{1-x}Ga_xAs$ superlattice. The growth is interrupted during the times (t_1,t_2,t_3,t_4), called a Growth-Interrupt-Sequence (GIS), as depicted in Figure 2.6. Here t_1 and t_3 are smoothening times and t_2 and t_4 are substitution times. The smoothening times are incorporated to let the surface rearrange itself, resulting in less roughness. During time t_2 P-atoms can be substituted by As-atoms. Additionally, the opposite process, namely As by P substitution can be introduced by t_4. For t_2 = 1 sec. approximately one ML of phosphorus is substituted by arsenic.

2.3 Substrate and Growth Mechanism

Substrates are bulk single crystals with extremely low defect densities and highly uniform properties in all crystallographic directions. All MBE samples are grown on semi-insulating exactly orientated InP substrates, i.e. the top surface of the substrate is a (100) surface. Generally, the MBE growth on exactly orientated substrates gives a low defect density and a good surface morphology for lattice matched structures.

Until recently, the CBE samples have been grown on exactly orientated substrates and on substrates 2° misorientated to (110). Although the exactly orientated substrates give a satisfactory structure quality for MBE, they give rise to defects for CBE. Therefore, for CBE also substrates with 2° misorientation to (110) are used. This misorientation gives rise to a different growth mechanism, for which such defects do not appear. However, for the substrates with 2° misorientation to (110), the morphology of the surface shows

macroscopic steps, which can be seen with an microscope. For device applications, defects or macroscopic steps can not be allowed and thus investigation of growth mechanisms on other misorientations is required.

On exactly orientated substrates the main growth mechanism is by 2 dimensional growth. This mechanism involves the creation of nucleus of atoms. These are islands which are one ML thick. If the islands have a lateral size smaller than a critical value, they disappear by desorption or evaporation of the constituent atoms, while islands that are larger expand in lateral direction. The islands expand until the regions between the islands are filled with atoms, after which the growth of the next layer begins. Thus this growth process leads to a roughness of the surface or interfaces in the order of one monolayer in the case the growth is interrupted before the last monolayer is completed. A roughness of a half monolayer means that only half of the available sites on the surface are occupied by atoms. However, during the stage in which the gaps between the islands are filled, nucleation on top of the islands is possible, leading to the simultaneous growth of a second monolayer. In this case a roughness of about two monolayers is present when the growth is stopped. Nevertheless, this only happens when the migration of the atoms over the surface is too small. The 2 dimensional growth does not give rise to problems for As containing layers grown with MBE. For CBE, however, a nucleation problem exists for the growth of InP, which gives rise to the defects mentioned above.

Next we discuss the growth mechanism on substrates with a miscut towards a defined direction. The misorientation leads to terraces separated by steps of one monolayer. This is shown in the side view of a substrate with 2° misorientation to (110), in Figure 2.7. For this misorientation the terraces are approximately 80 Å in length. During growth atoms are mainly incorporated at sites at the lower side of the steps (indicated by the arrows in Figure 2.7), which results a 'flow' of the steps as depicted in Figure 2.7. The major advantages compared to 2 dimensional growth are the larger growth rate and a more orderly lateral growth for InP, which results in an almost defect free morphology. However, a new phenomenon can appear for step-flow-growth, namely step bunching. Step bunching involves the accumulation of steps due to the retardation of the flow of the steps on the surface. This eventually gives rise to the macroscopically visible steps, mentioned above.

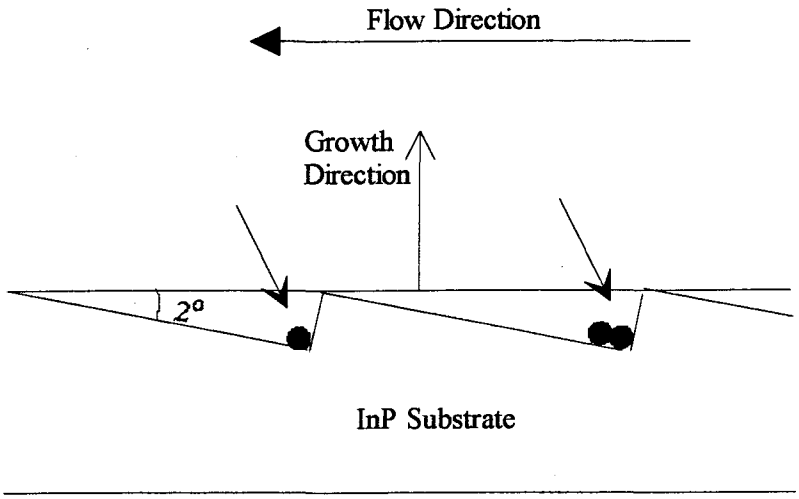

Figure 2.7: Schematic detail of the terraces and steps of a substrate with 2° misorientation to (110).

The misorientations of the substrates investigated for the CBE growth in this work are listed in table 2.1. The misorientations to (111)A and (111)B differ in the way that A-steps are terminated by group III atoms and B-steps by group V atoms.

Table 2.1: The various misorientations with their properties: angle terrace length and indication for steps/kinks. These misorientations are only used for the samples grown with CBE.

misorientation [°]	direction	terrace length [Å]	steps
0.5	(111)A	320	steps group III rich
0.5	(111)B	320	steps group V rich
2.0	(110)	80	mixed steps
0.5	(110)	320	mixed steps

2.4 Samples

In this section we describe the layer structures of the samples, according to the growth menu. We start with the description of the samples grown with MBE after which we focus on the samples grown with CBE.

The structure of the MBE samples is depicted in Figure 2.8. The substrate was submitted to the annealing procedure described in section 2.2, with an annealing time, which is listed in table 2.2 together with the sample-codes. After that a 0,25 μm thick bulk lattice matched $In_xAl_{1-x}As$ layer was grown. Because of the penetration depth of the laser light in the $In_xAl_{1-x}As$ layer, we had to etch approximately 0,20 μm of the layer away in order to be able to perform Raman measurements on the InAs interface.

The CBE samples were grown on various substrate orientations. In principle two basic structures have been grown, namely an InAs/InP superlattice (sample C382-x series) and an $In_{1-x}Ga_xAs$/InP superlattice (all other samples). The first is depicted in Figure 2.9a and the latter in Figure 2.9b (next page). Both superlattices are grown on a 0,5 μm InP buffer layer, which is grown directly on the substrate. The constituent layer pair for the InAs/InP superlattice consists of an InAs layer, formed by substitution of P by As-atoms for 1 sec. (1 ML InAs), and a 6 nm thick InP layer. A stack of 10 of these layer pairs forms the superlattice. The $In_{1-x}Ga_xAs$/InP superlattice consists of a same stack, with the difference that InP layer is 10 nm thick and the InAs layer is replaced by an $In_{1-x}Ga_xAs$ layer, which is 5 nm thick. Between the $In_{1-x}Ga_xAs$ and the InP layers, interfaces are formed due to a GIS (section 2.2). Samples have been grown with 4 different GIS's and on 5 different substrate orientations. The C386-x series is grown with a GIS = (2,1,2,1), but also a little gallium, indium and phosphorus is offered to the

Table 2.2: MBE sample names with annealing time.

sample code	t_{anneal} [min]
W677	4
W694	1
W695	2
W696	3
W697	4

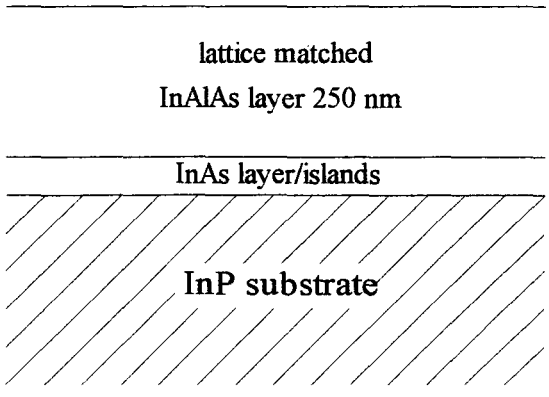

Figure 2.8: layer structure of MBE samples.

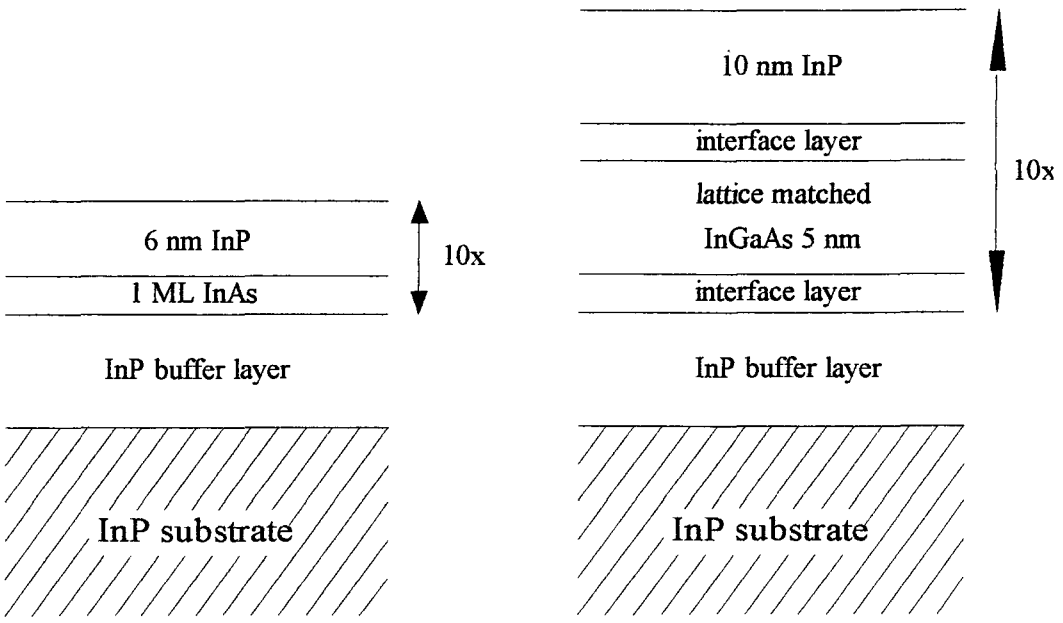

Figure 2.9a (left) layer structure of an InAs/InP superlattice and **2.9b (right)** the layer structure of an $In_{1-x}Ga_xAs$/InP superlattice. The structures are explained in the text.

surface at the interfaces. The various misorientations and GIS's are given table 2.3, in which also the sample code is listed.

Raman measurements were performed on all samples grown with MBE (table 2.2) and the following samples grown with CBE: C382-1 to C382-5, C385-1 to C385-5 and C383-5 to C386-5. Thus two sample series with the same layer structure but with different misorientation and one sample series with different growth interrupt sequences but with the same misorientation.

Table 2.3: sample names for CBE samples with various GIS's and different misorientations.

Misorientation	1 sec. subst.	GIS=(2,1,2,0)	GIS=(2,0,2,0)	GIS=(2,0,2,1)	GIS=(2,1,2,1)
2° to (110)	C382-1	C383-1	C384-1	C385-1	C386-1
0°	C382-2	C383-2	C384-2	C385-2	C386-2
0.5° to (110)	C382-3	C383-3	C384-3	C385-3	C386-3
0.5° to (111)A	C382-4	C383-4	C384-4	C385-4	C386-4
0.5° to (111)B	C382-5	C383-5	C384-5	C385-5	C386-5

3. Lattice Dynamics

Before we discuss Raman-spectroscopy, we first have to consider the lattice dynamics of a crystal. Generally in Raman-spectra of undoped semiconductors we encounter features as a consequence of various excitations of the crystal lattice. These excitations are mainly phonons, each representing a quantum of crystal vibrational energy, comparable to a photon which represents a light quantum. To be able to understand the aspects of phonons we present an overview of models on the vibrational modes in crystals. As described in [14], we start with the straight forward description of a lattice consisting of a monatomic basis in one dimension, in the harmonic approximation (3.1). Next, we extend our model for lattices with two different atoms per primitive (diatomic) basis (3.2). Following this procedure we have derived the basis for a model. This model in one dimension, already incorporates the basis phenomena required to understand crystal excitations (phonons) in 3-dimensional (real) lattices with a diatomic basis (3.3). Then we present a model describing phonon frequencies in ternary mixed compound crystals, like $In_{1-x}Ga_xAs$, with respect to the frequencies in the corresponding binary materials, InAs and GaAs crystals (3.4). Finally, in the last paragraph of this chapter we discuss the strain influence on the phonon frequencies (3.5).

3.1 Monatomic Linear Chain

To understand the dynamics of a monatomic linear chain one has to model the atoms in a lattice and the interactions between them. This can be achieved by visualising the subsequent atoms in a crystal lattice as a linear chain of atoms of mass m, bound to each other by the force due to Lennard-Jones potential. However, it is difficult to obtain any information based on this model, even when considering only one pair of potentials of the Lennard-Jones form. Therefore one uses the approximation that the atoms will not deviate substantially from their equilibrium positions. Furthermore, we assume that the elastic response of the crystal is a linear function of the force (Hook's Law). This last assumption is equivalent to the statement that the elastic energy is a quadratic function of the relative displacement of any two atoms in the lattice and is therefore called the harmonic approximation. The problem of lattice dynamics in this approximation is to find the normal modes of a crystal, which are the result of a normal coordinate transformation. The advantage of this transformation is that the motions of the atoms

are decoupled into noninteracting collective oscillations. An equivalent formulation of this problem is that one has to calculate the energies or frequencies of the phonons as a function of their wave vectors q, the phonon dispersion.

So far we considered the atoms in the crystal lattice as a system of harmonic coupled oscillators. For a linear crystal with N unit cells with each l atoms this results in Nl coupled differential equations. It is clear that it is a tough job to come to a solution and it is only due to the translation invariance of the lattice that we easily can. Nevertheless, for simplicity we assume that only nearest-neighbour forces are significant. Furthermore, we use periodic Born-von Kármán boundary conditions in one dimension, i.e. the chain is

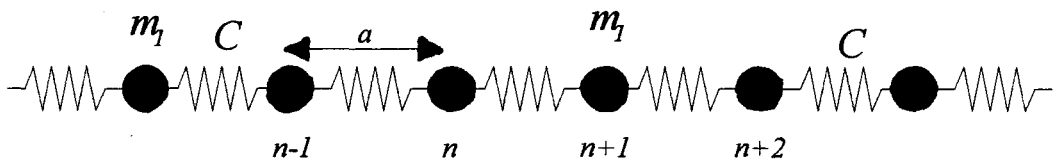

Figure 3.1: A monatomic linear chain with atoms which have mass m and spring constant C.

closed or bent into a ring. In equilibrium the atoms are separated by a distance of the lattice constant a, as shown in Figure 3.1. Suppose that the nth atom has a displacement u_n from its equilibrium position at time t. Application of Newton's second law and Hooke's Law this result in the following equation of motion:

$$m\frac{d^2u_n}{dt^2} = C\cdot(u_{n+1}-u_n)+C\cdot(u_{n-1}-u_n) \qquad (3.1)$$

where m is the mass of an atom and C is the nearest-neighbour force constant. Since we look for solutions with time dependence $e^{-i\omega t}$ we try:

$$u_n = A\cdot e^{i(qx-\omega t)} = A\cdot e^{i(qna-\omega t)} \qquad (3.2)$$

with x equal to na while A represents the amplitude of the vibration of the nth atom, q the wavenumber and ω the frequency of the phonon.

When equation (3.2) is substituted in equation (3.1), we obtain the 'eigenvalue' equation of the problem:

$$\omega^2 A = \frac{2C}{m}(1 - \cos qa)A \qquad (3.3)$$

which gives for $A \neq 0$ the solution:

$$\omega = 2\sqrt{\frac{C}{m}} \cdot \left| \sin \frac{qa}{2} \right| \qquad (3.4)$$

This dispersion relation is depicted in Figure 3.2. Note that the waves propagating in both directions ($\pm q$) are identical. Obviously, the displacement u_n and the phonon frequency ω are periodic in q, with periodicity $2\pi/a$. This periodicity in reciprocal space is directly due to that in real space, namely the translation invariance of the crystal lattice. Consequently, we only have to consider a small part of Figure 3.2, as a phase difference of more that π between two adjacent atoms makes no sense.

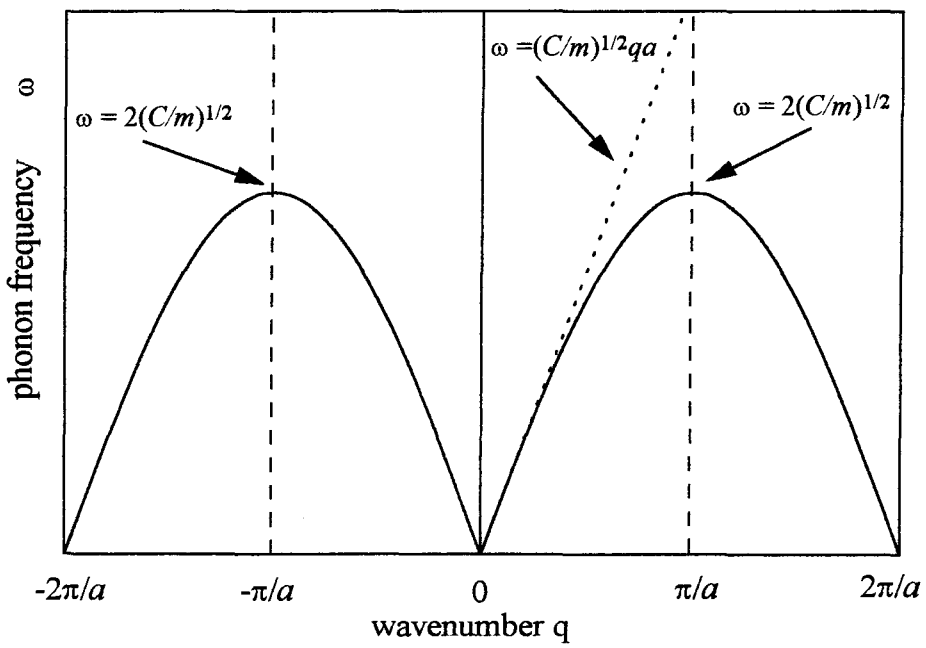

Figure 3.2: Dispersion relation of the monatomic linear chain. The entire figure is described in the text.

This also follows from the ratio between the displacements of two adjacent atoms:

$$\frac{u_{n+1}}{u_n} = e^{iqa} \qquad (3.5)$$

Obviously, all possible q values are covered by $-\pi/a \leq q \leq \pi/a$. This interval is the so-called first Brillouin zone.

Two regions in the phonon dispersion curve, as shown in Figure 3.2, are noteworthy. Using equation (3.4) for long wavelengths or small q values, the dispersion relation between ω and q becomes:

$$\omega = \sqrt{\frac{C}{m}} \cdot qa \qquad (3.6)$$

At these long wavelenghts many atoms are vibrating simultaneously with a small phaseshift between adjacent atoms. Therefore the discrete nature of the crystal lattice does not reveal itself. This describes exactly acoustic waves or sound waves in a continuum. Then equation (3.1) is nothing more than a simple wave equation and can directly be obtained by regarding the displacement u as a continuous function of x and expanding it in a Taylor-series:

$$\frac{1}{v^2}\frac{\partial^2 u}{\partial t^2} = \frac{\partial^2 u}{\partial x^2} \qquad (3.7)$$

with v the sound velocity given by $v=Ca^2/m$.

In the case of decreasing wavelength, which is equivalent to increasing q, the curve deviates from the linear relationship given by equation (3.6). The typical value of the wavelenght for which this becomes significant is in the order of the interatomic distance a. In other words the discrete structure of the chain becomes important. At the Brillouin zone boundary, where $q=\pm\pi/a$, the phase of vibrations of two neighbouring atoms differ by π, so the lattice wave becomes a standing wave with wavelength $\lambda = 2\pi/q = 2a$.

This situation is equivalent to the first order Bragg's reflection condition, given in three dimensions by:

$$\lambda = 2a \cdot \sin\theta \qquad (3.8)$$

where the angle of incidence θ is equal to 90 degrees in this case. Wavelengths shorter than $\lambda = 2a$ cannot propagate through the solid. However a wave motion with wavelength shorter than $2a$ is not meaningless, but is entirely equivalent to a wave of wavelength greater than $2a$.

3.2 Diatomic Linear Chain

The monatomic linear chain, described in the preceeding paragraph, is the simplest system of atom vibrations to study. Nevertheless, its dispersion provides fundamental understanding of the normal modes (dynamics) in a monatomic crystal. However the III/V semiconductors studied in this work consist of crystals with two or even more atoms per primitive basis. Therefore in this paragraph we extend our model of the dynamics of the monatomic linear chain to the diatomic linear chain which can be considered as a linear chain with a basis of two atoms.

Consider a chain of $2N$ atoms forming N unit cells. The unit cells are each $2a$ in length, as shown in Figure 3.3. Assume the chain to be closed so that

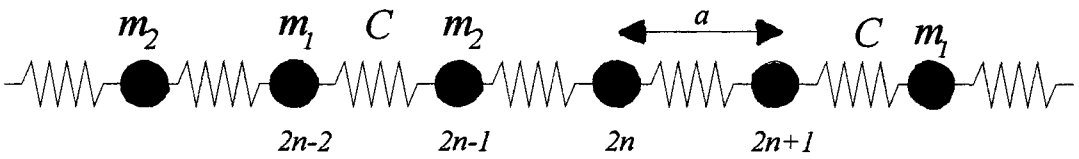

Figure 3.3: A diatomic linear chain with alternating masses m_1 and m_2 and spring-constant C.

we have periodic boundary conditions. Let m_1 and m_2 be the masses of the individual atoms in the basis, with m_1 smaller than m_2. Further, we assume that each type of atom is coupled by identical springs (spring constant C) to its neighbours and that only nearest neighbour forces are significant. Then, analog to the monatomic chain, the equations of motion for the two types of atom become:

$$m_1 \frac{d^2 u_{2n}}{dt^2} = C \cdot (u'_{2n+1} - u_{2n}) + C \cdot (u'_{2n-1} - u_{2n}) \qquad (3.9a)$$

$$m_2 \frac{d^2 u'_{2n+1}}{dt^2} = C \cdot (u_{2n+2} - u'_{2n+1}) + C \cdot (u_{2n} - u'_{2n+1}) \qquad (3.9b)$$

with u and u' the displacements of the atoms from their equilibrium positions with a mass of m_1 and m_2 respectively. As shown in Figure 3.3, the atoms with mass m_1 are positioned at the even lattice points while the other atoms are positioned at the odd ones. We expect the atoms from one type to have the same amplitude, while those of the other type have a different amplitude. Further we expect a solution which varies from cell to cell. Therefore let us try the solutions:

$$u_{2n} = A_1 \cdot e^{i \cdot 2nqa} \cdot e^{-i\omega t} \qquad (3.10a)$$

$$u'_{2n+1} = A_2 \cdot e^{i(2n+1)qa} \cdot e^{-i\omega t} \qquad (3.10b)$$

From substitution of equation (3.10) in equation (3.9) the following set of coupled eigenvalue equations is found:

$$-\omega^2 m_1 A_1 = C \cdot \left[A_2 e^{iqa} + A_2 e^{-iqa} - 2A_1 \right] \qquad (3.11a)$$

$$-\omega^2 m_2 A_2 = C \cdot \left[A_1 e^{-iqa} + A_1 e^{iqa} - 2A_2 \right] \qquad (3.11b)$$

They can be rewritten in the form:

$$\omega^2 A_i = \sum_{j=1}^{2} D_{ij} A_i \quad , \; i = 1,2 \qquad (3.12)$$

with D a (2x2) matrix. Non-trivial solutions ($A \neq 0$) are given by solving the equation:

$$\left| D_{ij} - \omega^2 \delta_{ij} \right| = 0 \qquad (3.13)$$

where δ_{ij} represents the Kronecker delta. The solutions are:

$$\omega^2 = C\cdot\left(\frac{1}{m_1}+\frac{1}{m_2}\right) \pm C\cdot\sqrt{\left(\frac{1}{m_1}+\frac{1}{m_2}\right)^2 - \frac{4}{m_1 m_2}\sin^2(qa)} \qquad (3.14)$$

the so-called dispersion relations. The amplitude ratio of the displacements is:

$$\frac{A_1}{A_2} = \frac{2C\cos(qa)}{2C - m_1\omega^2} = \frac{2C - m_2\omega^2}{2C\cos(qa)} \qquad (3.15)$$

Corresponding to the two signs in equation (3.14) there are two branches of the phonon dispersion curve $\omega(q)$ for the diatomic linear chain and each represents a separate solution with periodicity π/a. These curves are depicted in Figure 3.4.

Next, we consider the two branches for long wavelengths (q is small; $qa \ll 1$). The signs of A_1 and A_2 are opposite for the upper branche of $\omega(q)$ in Figure 3.4. This means that the two atoms in the unit cell move in opposite direc-

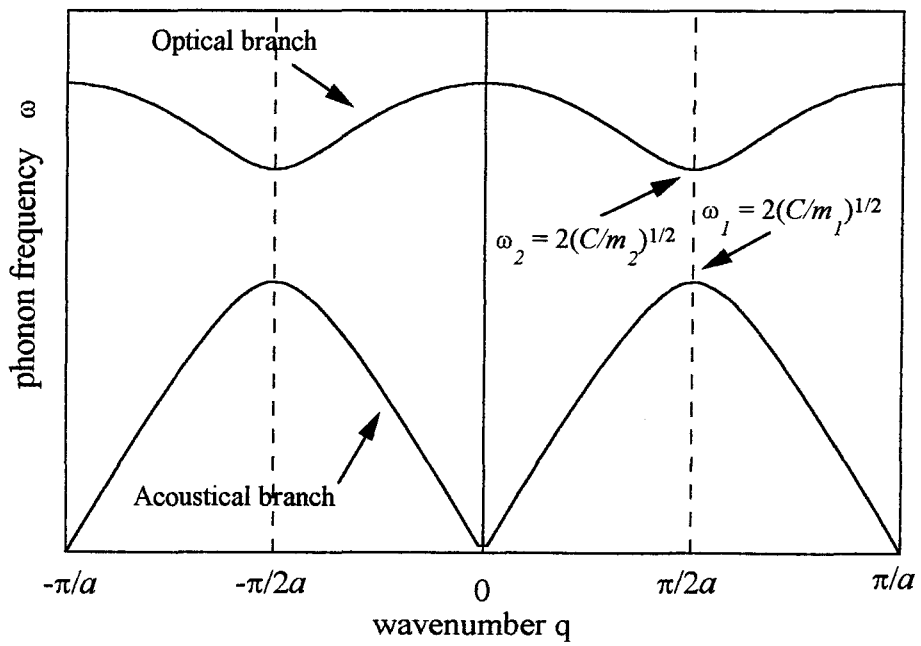

Figure 3.4: Dispersion relation for a diatomic linear chain with masses m_1 and m_2 and springconstant C. All symbols are explained in the text.

tions. If the atoms have opposite charges, such a mode creates a set of oscillating dipoles. On the other hand this mode can be induced by an electric field of the appropriate frequency. In most solids this frequency corresponds to that of infra-red light. Therefore this branche is also called the optical branch, and the associated crystal vibrations optical phonons.

For small q in the lower branch $A_1/A_2 \approx 1$ and thus both atoms in the unit cell move in phase. These are the conditions for sound waves to appear in solids which is analogous to the monatomic linear chain.. Hence the lower branch is indicated as the acoustical branch. In agreement with the monatomic case, for small q the detailed structure of the chain has no effect on the mode (wavelenght » interatomic spacing) and ω is proportional to q. Away from the zone centre where q equals zero, for finite values of q, there is no obvious distinction between the vibrational modes of the acoustic and optical branches since the detailed structure of the chain becomes more visible.

Note that at the brillouin zone boundaries ($q=\pm\pi/2a$) ω is given by:

$$\omega_i = \left(\frac{2C}{m_i}\right)^{1/2}, \quad i = 1,2 \qquad (3.16)$$

When we substitute equation (3.16) in equation (3.15) we obtain:

$$\frac{A_1}{A_2} = \frac{2C - m_2\omega^2}{2C\cos(qa)} \rightarrow \infty \qquad (3.17a)$$

$$\frac{A_1}{A_2} = \frac{2C\cos(qa)}{2C - m_1\omega^2} = 0 \qquad (3.17b)$$

In other words at ω equal to ω_2 (in equation 3.17a), the atoms with the heavier mass (m_2) are not moving: $A_2 = 0$. Further, in equation (3.17b) , at ω equal to ω_1 atoms with the lighter mass (m_1) are not moving: $A_1 = 0$. For both situations the wave is stationary. Thus, there is no propagation of waves through the solid at these frequencies. Between these frequencies no wave-like solutions exist. The solutions with ω real result in an imaginary value of q, which is in physical sense a wave damped in space.

If we look at the case in which m_1 approaches m_2, the dispersion of the diatomic chain becomes similar to that of the monatomic chain. This is as

expected since the physical difference between the two chains is lifted, which is also reflected in the phonon dispersion curve. As for the case that m_1 approaches m_2, the gap at $q = \pi/a$ which was due to the the mass difference between the two types of atoms disappears, while the top branch unfolds to cover the q-regions $\pi/2a$ to π/a and $-\pi/2a$ to $-\pi/a$.

3.3 3-Dimensional Crystals

The method based on the interatomic force constants used in the preceeding two paragraphs for the one-dimensional case, can be extended to obtain the normal modes of a general three dimensional crystal. However, one of the main problems in lattice dynamics is the determination of the force constants, even though the number of independent ones is limited by the lattice symmetry. Therefore one resorts to various models for interatomic force constants, which is beyond the scope of this work. For more details we refer to some text books on advanced solid state physics [14,15,16]. Instead, we use a more qualitative description of the different phonon modes.

Let us assume a crystal with p atoms per unit cell, which results in $3p$ phonon branches in the phonon dispersion curve. Three of them are acoustic branches and correspond to the three possible vibrational modes, namely one longitudinal and two transverse. For the acoustical branches applies that $\omega(\boldsymbol{q})$ approaches zero when $\boldsymbol{q} \rightarrow \boldsymbol{0}$. Since there are 3 acoustical branches, there must be $3p$-3 optical branches, for which $\omega(\boldsymbol{q})$ reaches a constant for $\boldsymbol{q} \rightarrow \boldsymbol{0}$.

In general, the atomic vibrations can be either longitudinal, transverse or a mixture of both. Only in an isotropic crystal it is possible that all polarisation modes occur independent from each other. Specifically, in cubic crystals pure transverse or longitudinal polarisation modes can only exist along the symmetry directions [111], [110] and [100]. For purely covalent crystals the optic modes are degenerate. In the case that the bonding has an ionic character, only the two transverse optical modes are degenerate, while the longitudinal optical mode has a slightly higher frequency. This is due to the electrostatic field created by the long-wavelength modes of vibration, which acts as an additional restoring force. The difference in frequency between the transverse optic (TO) modes and the longitudinal optic (LO) mode is called the 'longitudinal-transverse splitting'. This splitting becomes larger with increasing ionicity of the bonds between the two types of atoms in the

unit cell and is related to the dielectric constant.. This will be shown in the following derivation (from [16]).

Again $\boldsymbol{u}$ is the amplitude of the displacement. Let the internal electric field in the crystal be $\boldsymbol{E}_{int}$. The following equation of motion for the modes results:

$$\frac{\partial^2 \vec{u}}{\partial t^2} = -\omega_o^2 \vec{u} + b\vec{E}_{int} \qquad (3.18)$$

where b is the coupling of the internal electric field $\boldsymbol{E}_{int}$ with the ions of the crystal, and ω_o is the frequency of the lattice vibration without ionic contribution to the bonds between the atoms. Meanwhile the displacement $\boldsymbol{u}$ will induce a polarisation density $\boldsymbol{P}$, which will be enhanced by the polarisation created by the electric field. Thus for $\boldsymbol{P}$ we obtain:

$$\vec{P} = (b'\vec{u} + \alpha\vec{E}_{int})\varepsilon_o \qquad (3.19)$$

with ε_0 the permittivity in vacuum, α the polarisabillity of the concerning atoms. The parameter b' gives the polarisabillity induced by the displacement $\boldsymbol{u}$. Equation (3.18) and (3.19) together with the Maxwell electrostatic equations and the divergence and curl of $\boldsymbol{u}$ for transverse waves gives us:

$$\frac{\partial^2 u_T}{\partial t^2} = -\omega_o^2 u_T \quad or \quad \omega_T^2 = \omega_o^2 \qquad (3.20)$$

In other words, the frequency of the transverse modes is unaffected by the electric field. However looking at the longitudinal waves, we obtain:

$$\frac{\partial^2 u_L}{\partial t^2} = -\left(\omega_o^2 + \frac{bb'}{1+\alpha}\right)u_L \qquad (3.21)$$

Using equations (3.18) and (3.19) we can write this equation more simply in terms of a dielectric constant:

$$\vec{D} = \varepsilon_o\vec{E}_{int} + \vec{P} = \varepsilon_o\left(1 + \alpha - \frac{bb'}{\omega^2 - \omega_o^2}\right)\vec{E}_{int} = \varepsilon_o\varepsilon_r(\omega)\vec{E}_{int} \qquad (3.22)$$

The expression in parentheses in (3.22) is the frequency dependent relative dielectric constant ε_r of the system. For $\omega \to \infty$, $\varepsilon_r(\omega)$ approaches its high frequency value $\varepsilon(\infty)$, given by:

$$\varepsilon(\infty) = 1 + \alpha \qquad (3.23)$$

while for $\omega \to 0$, $\varepsilon_r(\omega)$ approaches its low frequency value $\varepsilon(0)$, given by:

$$\varepsilon(0) = \varepsilon(\infty) + \frac{bb'}{\omega_o^2} \qquad (3.24)$$

With these expressions we can rewrite equation (3.22) in a more comprehensive form:

$$\varepsilon_r(\omega) = \varepsilon(\infty) + \omega_o^2 \frac{\varepsilon(0) - \varepsilon(\infty)}{\omega_o^2 - \omega^2} \qquad (3.25)$$

Using the same expressions in (3.21) one can obtain the longitudinal mode frequency ω_L ,through the relation:

$$\omega_L^2 = \frac{\varepsilon(0)}{\varepsilon(\infty)} \omega_T^2 \qquad (3.26)$$

This important relationship is called the Lyddane, Sachs, Teller (LST) rela-

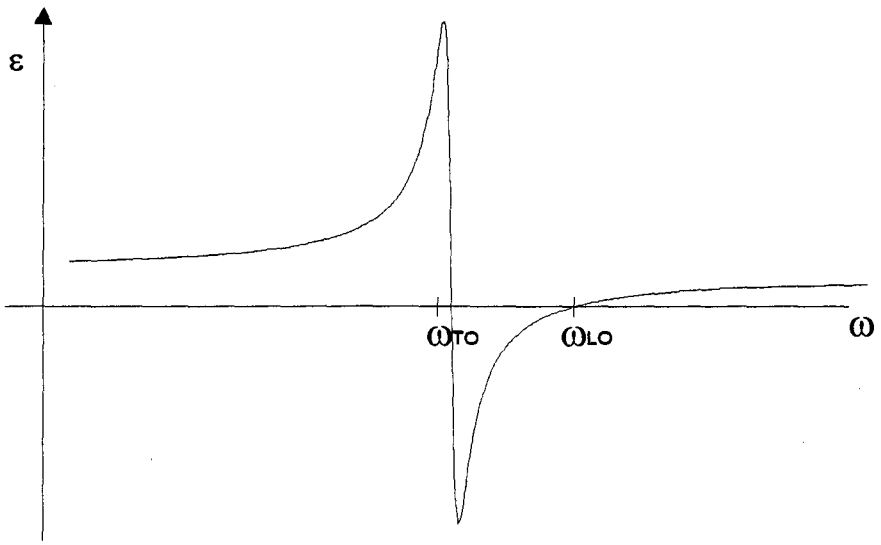

Figure 3.5: Real part of the dielectric function for a polar crystal, according to the Born-Huang model.

tion. With $\omega_o = \omega_T$ and the LST-relation, equation (3.25) becomes:

$$\varepsilon_r(\omega) = \varepsilon(\infty)\frac{\omega_L^2 - \omega^2}{\omega_T^2 - \omega^2} \qquad (3.27)$$

For this $\varepsilon_r(\omega)$ the real part is depicted in Figure 3.5, where also damping is included, as in real crystals (Born-Huang model). Clearly, from (3.27) the dielectric constant becomes infinite at $\omega = \omega_T$ and is negative when $\omega_T < \omega < \omega_L$, which means that incident electromagnetic waves (light) of these frequencies do not propagate in the medium, but are reflected at the boundary. This reflection is the so-called 'Reststrahlen'-reflection.

For $\varepsilon(0) = \varepsilon(\infty)$, we obtain $\omega_L = \omega_T = \omega_o$ and $\varepsilon_r = \varepsilon(\infty) =$ constant. This is the case for purely covalent bonds for which no ionic contribution to ε_r ($b = b' = 0$) is present, and thus all the optic modes are degenerate. From equation (3.26) it is obvious that a larger difference between $\varepsilon(\infty)$ and $\varepsilon(0)$, i.e. a more ionic bond, leads to a increased splitting between ω_L and ω_T. For most solids $\varepsilon(0) > \varepsilon(\infty)$ and thus $\omega_L > \omega_T$ (see Figure 3.5).

3.4 Mixed Crystals

Sofar we only discussed phonons in binary compounds. Here we continue with the description of the model for the phononfrequencies in ternary semiconducting material with respect to their constituent binary compounds.

Consider a ternary compound $A_{1-x}B_xC$ with $x<<1$, i.e. there is only a small concentration of the B-atom in the compound AC, the host crystal. Considering the dynamics of such a system, there is the possibility of one- and two-mode behaviour. The simplest case is the one-mode behaviour for which only one set of optical frequencies is found. In a first approximation these frequencies vary linearly with the composition x from the values for the binary AC to that of the other BC (see Figure 3.6a). This is only possible when the mass difference between the A- and the B-atom is small enough. In other words, if the frequency of the minority atom (B) is in the optical frequency range of the host crystal AC, it is possible for both the crystal vibrations to couple. However, when the phonon frequency of the B-atom can not couple to the optical modes of the host crystal, i.e. the mass difference between the A- and the B-atom is too large, we obtain a two-mode behaviour. In the latter case two sets of (long wavelenght) optical phonons

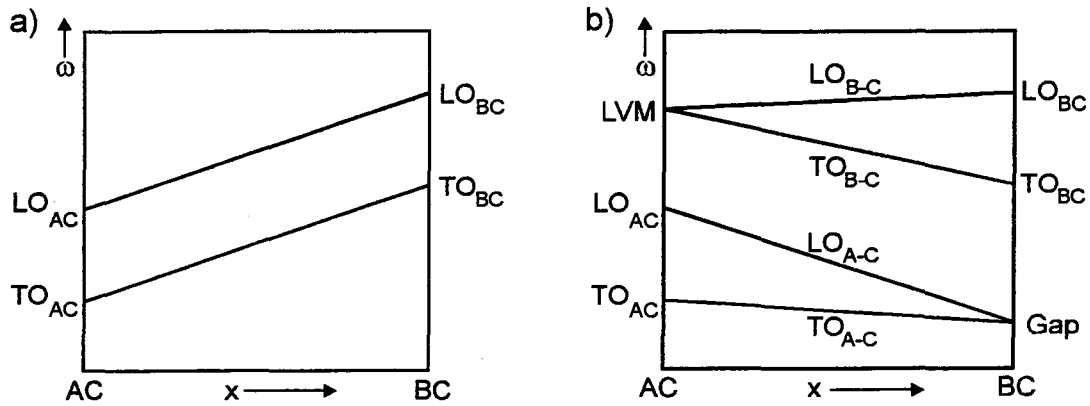

Figure 3.6a (left) LO and TO frequency for one mode behaviour and **3.6b** (right) LO and TO frequency for two mode behaviour (both gap-mode and local-vibrational mode).

close to those of the constituent binary crystals are possible for a given composition x (see Figure 3.6b). Explicity, in a ternary compound like $In_{1-x}Ga_xAs$, which exhibits two-mode behaviour, this results in two LO-TO pairs. They are indicated as the InAs-like mode and the GaAs-like mode. When the frequency of the vibration mode of the B-atom is above the optical modes of the host crystal, it is called a 'local-mode', and a 'gap-mode' if its frequency is situated between the optical and acoustic modes of the host crystal.

A practical convenient criterion on the expectation of a mixed crystal to have one-mode or two-mode behaviour, is the MREI-model (Modified-Random-Element-Isodisplacement) [17]. From this model follows that if for a mixed crystal $A_{1-x}B_xC$ the mass of atom B is smaller than the reduced mass of the binary AC, then the mixed crystals exhibits two-mode behaviour, i.e.:

$$m_B < \mu_{AC} \text{ gives a two-mode behaviour with } m_B < m_A \qquad (3.28)$$

where μ_{AC} is the reduced mass of the atoms A and C, and m_B is the mass of the B-atom. If the mass of the substituting element B is larger than this reduced mass, the system exhibits one-mode behaviour.

As pointed out before the phonon frequencies in mixed crystals depend on the composition, which enables us to derive it from the position of the phonon peaks associated with one- or two-mode behaviour. However, one should be very carefull as the frequencies can also be modified by strain in the crystal. Therefore we discuss the influence of strain on phonon frequencies in the next paragraph.

3.5 Strain and Phonon Frequencies

As discussed in chapter 1, strain can be present in pseudomorphic structures. The relative mismatch in the material investigated in this work, is typically more than 1 percent, which is large . For example, InAs on InP gives a mismatch of more than 3 percent, resulting in a critical thickness of a few monolayers.

In this section we discuss the features which arise in Raman spectra due to strain. Since stress induced lattice deformation affect the lattice dynamics, we expect the phonon frequencies to shift. The strain (tensor) is given by Hook's law [18]:

$$\vec{\vec{\varepsilon}} = \vec{\vec{S}} \cdot \vec{\vec{\sigma}} \qquad (3.29)$$

Where ε is the relative mismatch of the lattice constants, σ the corresponding pressure and $\boldsymbol{S}$ the modulus or compliance. The latter is dependent on elastic constants and therefore characteristic for the material. The relation between the phonon frequencies and the strain tensor is described by the phonon deformation potential tensor. All III/V semiconductors which appear in this work consist of a cubic lattice, yielding three independent non-zero components for this tensor, called p, q and r.

For a pseudomorphic strained layer the lattice constant parallel to the interface $a_{//}$ must be equal to the substrate lattice constant a_S. The mismatch between these lattice constants leads to a strain component parallel to the interface. Using equation (1.2) we obtain:

$$\varepsilon_{//} = \varepsilon_{xx} = \varepsilon_{yy} = \frac{a_S - a_L}{a_L} \qquad (3.30)$$

The lattice constants in this equation are relaxed values. This strain induces a tetragonal distortion as described in chapter 1, yielding a strain component in the layer, perpendicular to the interface:

$$\varepsilon_{\perp} = \frac{2S_{12}}{S_{11} + S_{12}} \cdot \varepsilon_{//} \qquad (3.31)$$

in this equation S_{ij} are the components of the compliance tensor.

The tetragonal distortion leads to a splitting of the three-fold degenerate phonon oscillator by means of the electronic deformation potentials. These are the same potentials which give rise to a splitting of light-hole and heavy-hole valence bands due to shear strain. The degenerate phonon oscillator splits into a singlet mode, with a lattice atomic displacement perpendicular to the interface, and a doublet mode with a lattice atomic displacement parallel to the interface. For the (100) back scattering geometry, the singlet mode is the LO phonon and the doublet mode is the TO phonon. Since for (100) back scattering the LO phonon is symmetry allowed and the TO phonon is not, the main effect of strain in Raman spectra is a shift of the LO phonon.

More generally, from group theory it is known that when the symmetry of the system is reduced from the cubic symmetry (unstrained case) to the orthorhombic symmetry (strained case), three-fold degeneracy's are no longer allowed. This means that due to symmetry reduction the three fold degenerated phonon oscillator must split into three non-degenerate oscillators or in one non-degenerate and one two-fold degenerate oscillator. The latter is the case. This can be made plausible, since the x,y plane (parallel to the interface) remains invariant under the symmetry reduction and thus a two-fold degeneracy is allowed.

The strain induced shift of the phonon frequencies can be calculated by means of the following equations [19]:

$$\Delta\omega_{LO} = \left(\frac{p+2q}{3\omega_0^2} \cdot \frac{(S_{11}+2S_{12})}{(S_{11}+S_{12})} + \frac{2}{3} \cdot \frac{q-p}{2\omega_0^2} \cdot \frac{(S_{11}-S_{12})}{(S_{11}+S_{12})} \right) \cdot \omega_0 \cdot \varepsilon_{//} \qquad (3.32a)$$

$$\Delta\omega_{TO} = \left(\frac{p+2q}{3\omega_0^2} \cdot \frac{(S_{11}+2S_{12})}{(S_{11}+S_{12})} - \frac{1}{3} \cdot \frac{q-p}{2\omega_0^2} \cdot \frac{(S_{11}-S_{12})}{(S_{11}+S_{12})} \right) \cdot \omega_0 \cdot \varepsilon_{//} \qquad (3.32b)$$

The III/V semiconductors have compliance tensor elements S_{11} in the range of $2 \cdot 10^{-11}$ Pa^{-1} and S_{12} in the range of $-1 \cdot 10^{-11}$ Pa^{-1} [19]. This results in phonon frequency shifts of about 3 percent for the allowed LO phonon and 1.5 percent for the TO phonon, when the lattice mismatch is about 3 percent, as in our example of InAs to InP.

Generally, in Raman spectroscopy we observe lattice mismatches beyond 0.1 percent for frequencies in the 300 cm^{-1} range. This follows from the inaccuracy in the determination of the positions of the Raman peaks. Thus

measuring strain with Raman spectroscopy is far less accurate compared to a X-ray diffraction (XRD). However, Raman spectroscopy provides us with some features not available in XRD-experiments. The most important one is undoubtedly the sensitivity for individual materials through the shift of their characteristic phonon frequencies.

4. Raman Spectroscopy

The principle of the Raman effect is based on inelastic light scattering. Light of a certain frequency impinges on a crystal, which induces different types of excitations. These excitations consist of phonons, plasmons, polaritons and excitations of a single electron or hole etc. We only discuss the Raman effect due to phonons.

Consider a crystal by which incident light with frequency ω_i is inelasticly scattered. The scattered light has frequency ω_s ($\omega_s \neq \omega_i$), which means there is a energy transfer between the incident photons and the crystal. This energy transfer, however, can not consist of any arbitrary amount of energy, but must correspond to an eigenvalue energy $\hbar\Omega_n$ of an elementary excitation in the crystal. For the entire scattering process, the energy conservation law is valid and represented by:

$$\hbar\omega_i = \hbar\omega_s \pm \hbar\Omega_n \qquad (4.1)$$

The '+' sign in this equation represents the creation of an excitation as described above and is referred to as a 'Stokes' process. The other case, the '-' sign, describes the annihilation of an elementary excitation which is called an 'anti Stokes' process. In most Raman studies Stokes processes are considered. Besides energy conservation, also quasi momentum is conserved in Raman scattering. This yields in a relation between the phonon momentum $\boldsymbol{q_n}$ and the wave vectors $\boldsymbol{k_i}$ and $\boldsymbol{k_s}$ of the incident and scattered light respectively. In back scattering geometry, where incident and scattered light are both (almost) perpendicular to the surface of the crystal, the quasi momentum conservation leads to a formula in the form:

$$\vec{q}_n = \vec{k}_i + \vec{k}_s \approx 2\vec{k}_i \qquad (4.2)$$

where $\boldsymbol{k_i} \approx \boldsymbol{k_s}$ is assumed. This assumption is reasonable since the energy transferred from the incident photon to the crystal is about one percent. Because the incident light is in the visible range this implies, that the wave vector $\boldsymbol{q_n}$ is relatively small with respect to $2\pi/a$, which means that $\boldsymbol{q_n}$ is very close to the centre of the Brillouin zone. In this wave vector domain, the optical phonon frequencies are independent of $\boldsymbol{q}$ as is obvious because there is little or no slope in the phonon dispersion in figure 3.4. Thus the optical phonon frequencies measured by Raman spectroscopy are independent

of the incident light frequency. The assumption that $\boldsymbol{q}$ is small does not apply to higher order Raman scattering (multiple phonon processes), since there could arise two phonons with larger $\boldsymbol{q}$ and opposite signs.

Besides inelastic scattered light, the scattering process on the crystal also gives rise to elastic scattered light (Rayleigh scattering). In an experimental set-up we prevent this light from entering the detection system by deliberately creating an angle of incidence of the impinging light beam. Thus we do not have an exact back scattering geometry. However, elastic scattered light due to diffuse scattered light caused by a dirty surface or the roughness of the surface itself, remains a problem in Raman spectroscopy. For acoustic phonons, which are extremely close to the laserline, this is the reason why they are normally not observed in Raman spectra.

The energy of optical phonons is higher, in the range of 20 to 50 meV for III/V semiconductors. Since normally light sources in the spectral visible range, 1.5 to 3 eV, are used, direct interaction of a photon with lattice vibrations is not possible. However, an indirect interaction occurs via electron transitions between valence and conduction bands, which act as intermediate states. This gives rise to the Raman effect since interband transitions are affected by the occurrence of a phonon.

We continue with the interaction between light and crystals in a macroscopic and a microscopic theory. Both theories are based on the dielectric susceptibility in order to determine the response of the crystal on incident light.

4.1 Macroscopic theory

In the macroscopic theory light scattering is described with the dielectric susceptibility, which couples the induced polarisation $\boldsymbol{P}$ to the electric field of the incident light $\boldsymbol{E_i}$:

$$\vec{E}_i = \vec{E}_o \cos(\vec{k}_i \cdot \vec{r} - \omega_i t) \qquad (4.3a)$$

$$\vec{P}(\omega_s) = \varepsilon_o \vec{\vec{\chi}}(\omega_i, \omega_s)\vec{E}(\omega_i) \qquad (4.3b)$$

where χ is the susceptibility tensor, which we assume only to be depended on ω_i and ω_s. The lattice vibration (phonon) induces a modulation of the susceptibility. This becomes clear when expanding the tensor components

$\chi_{\alpha\beta}(\omega_i,\omega_s)$ of the dielectric susceptibility into a Taylor series in terms of the phonon normal coordinates. We assume the dielectric susceptibility to be independent of time and place in the crystal:

$$\chi^{\alpha,\beta}(\omega_i) = \chi_o^{\alpha,\beta}(\omega_i) + \sum_k \frac{\partial \chi^{\alpha,\beta}}{\partial Q_k} Q_k + \sum_{k,l} \frac{\partial^2 \chi^{\alpha,\beta}}{\partial Q_k \partial Q_l} Q_k Q_l + \ldots \qquad (4.4a)$$

$$Q_j = Q_{j,o} \cos(\vec{q}_j \cdot \vec{r} - \Omega_j t) \qquad (4.4b)$$

with Ω_j the phonon frequency, Q_j^o the amplitude of the lattice deformation, and q_j the corresponding wave vector of the jth mode; α and β are the polarisation of the scattered and the incident light and the associated electric fields. Note that we used the assumption $\omega_i \approx \omega_s$ in the Taylor expansion. The first term in equation (4.4a) represents the elastic or Rayleigh scattering, of the incident light on the crystal. The second term describes the dependence of the susceptibility on lattice deformations. The third term represents a scattering process in which two phonons occur, i.e. a two phonon process. For one phonon processes we obtain a polarisation, with equation (4.4a) and equation (4.3b):

$$P^{\alpha} = \varepsilon_o \sum_k \frac{\partial \chi^{\alpha\beta}}{\partial Q_k} Q_k E_i^{\beta} \qquad (4.5)$$

using equation (4.4b), i.e. phonon normal coordinates, this results in:

$$P^{\alpha} = \frac{\varepsilon_o}{2} E_o^{\beta} \sum_k \frac{\partial \chi^{\alpha\beta}}{\partial Q_k} Q_{k,o} \Big[\cos\big((\vec{k}_i + \vec{q})\vec{r} - (\omega_i + \Omega)t\big) + \cos\big((\vec{k}_i - \vec{q})\vec{r} - (\omega_i - \Omega)t\big) \Big] \qquad (4.6)$$

where E_o^{β} represents the amplitude of the electric field. It can be concluded that the polarisation P^{α} is dependent on the frequencies $\omega_i \pm \Omega$. Meaning there will occur two Raman lines, namely at frequency $\omega_i - \Omega$ (Stokes) and frequency $\omega_i + \Omega$ (anti Stokes).

Obviously, the processes involved here are second order effects and thus the intensities of the Raman lines will be lower than the intensity of the Rayleigh line (10^4 to 10^8 lower intensity). However, with the classical theory we are

not able to explain the intensity ratio between the Stokes line and the anti-Stokes line, which is given by the classical result for the intensity of dipole radiation:

$$\frac{I_{Stokes}}{I_{anti-Stokes}} = \frac{(\omega_i - \Omega)^4}{(\omega_i + \Omega)^4} < 1 \qquad (4.7)$$

According to this equation the Stokes line should be weaker in intensity when compared to the anti-Stokes line. Yet in measurements we observe the opposite, the Stokes line is always stronger in intensity when compared to the anti-Stokes line. Therefore, an alternative theory is required which excludes this inconsistency.

4.2 Microscopic theory

The Raman scattering process discussed in the preceeding paragraph can also be described in quantummechanical perturbation theory (electron-photon and electron-phonon interaction). Consider a photon of energy $\hbar\omega_i$ impinging on the crystal. There is a finite probability that the photon is annihilated and excites an electron from a ground state |0> to a state |e>, in the conduction band (figure 4.1b). Interaction between crystal lattice and electron is possible and results in a transition to a different electronic state |e'> accompanied by the emission of a phonon of energy $\hbar\omega_{ph}$. Then recombination of the electron hole pair is likely by emission of a photon $\hbar\omega_s$. After that, the electron is in its initial ground state again. The Feynman diagram of the entire scattering process is depicted in figure 4.1a. For the process described above, the dielectric susceptibility can be calculated by third order perturbation theory [20]:

$$\chi^{\alpha,\beta} \propto \sum_{e,e'} \frac{\langle o|p_\alpha|e'\rangle\langle e'|H_{E\text{-}L}|e\rangle\langle e|p_\beta|o\rangle}{(E_{e'} - \hbar\omega_s)(E_e - \hbar\omega_i)} + \ 5\,permutations \qquad (4.8)$$

where $H_{E\text{-}L}$ is the Hamiltonian of the electron-phonon interaction while p_α and p_β are vectorcomponents of the dipole operators for the scattered and incident light. Energies of the excited states are called E_e and $E_{e'}$. The two terms $< 0 \mid p_\alpha \mid e' >$ and $< 0 \mid p_\beta \mid e' >$ describe the photon-electron interaction, while $< e' \mid H_{E\text{-}L} \mid e >$ corresponds to the electron-phonon interaction.

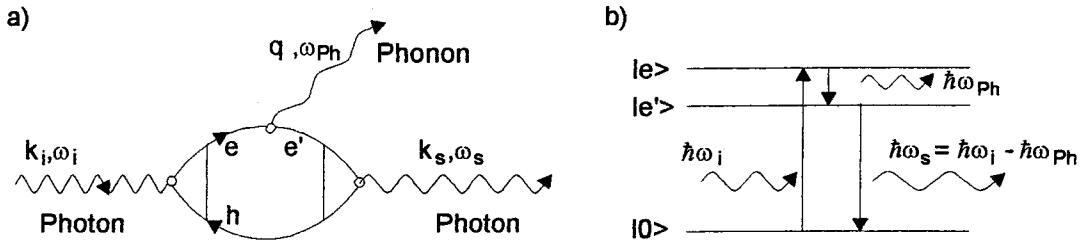

Figure 4.1a (left) Feynman diagram for the inelastic light scattering process and **4.1b** (right) the corresponding energy transitions.

For the entire process energy is conserved. However, for the individual transitions the energy is nearly conserved, as a result of the time-energy Heisenberg relation. Thus a transition from state | 0 > to state | e > is also possible for energies $\hbar\omega_i$ smaller than E_e. In that case a virtual electron-hole pair arises which recombines within the time imposed by the uncertainty relation. Another consequence of the uncertainty relation is that the scattering process mentioned above need not occur in that specific order. That explains why there are five more permutations in equation (4.8) corresponding to the permutations of the three factors in the numerator. It should be noticed that when the energy difference between the state | 0 > and the state | e > decreases, the transition and thus the creation of a phonon becomes more probable. As the energy difference approaches zero, i.e. the energy of the incident light reaches a specific energy transition of the material, the denominator in equation (4.8) is approximately zero and thus the components of the susceptibility tensor increase rapidly. This leads to a resonance behaviour of the transition which results in a steep increase of the intensity of the Raman line, for instance at the energy gap for III/V semiconductors.

Now we reconsider the inconsistency found in the previous section concerning the intensity ratio between the Stokes and the anti-Stokes line for optical phonons. We found that the anti-Stokes line is higher in intensity according to the classical result for dipole radiation. However, in experiments the Stokes line generally appears to be higher. This contradiction is a result of not including the statistics of phonon states, i.e. the Bose-Einstein distribution [16]:

$$n = \frac{1}{e^{\frac{\hbar\Omega}{kT}} - 1} \qquad (4.10)$$

here n is the number of phonons at temperature T and k is the Boltzmann constant. With this relation it becomes clear that the intensity of the Stokes-line has to be higher with respect to the intensity of the anti-Stokes line. The occupation of the ground state is much higher compared to the occupation of the excited states. With equation (4.10) and quantum theory the intensity ratio becomes:

$$\frac{I_{Stokes}}{I_{anti-Stokes}} = \frac{(\omega_i - \Omega)^4}{(\omega_i + \Omega)^4} \cdot \frac{1-n}{n} = \frac{(\omega_i - \Omega)^4}{(\omega_i + \Omega)^4} \cdot e^{\frac{\hbar\Omega}{kT}} > 1 \qquad (4.11)$$

This result is in agreement with experimental results. However, the '>' in this equation is only applicable when the temperature T is not too high ($kT < \hbar\Omega$). In general the intensity of the Stokes line is higher and therefore used for measurements. The Raman spectra presented in this work were all recorded by measuring the Stokes line.

4.3 Symmetry and Selection Rules

In this paragraph we discuss the conditions for interaction between a optical phonon and a photon, imposed by symmetry considerations and the associated selection rules. The symmetry of the crystal defines which lattice vibrations are allowed for the different polarisations of the incident and scattered light. In other words, symmetry gives the conditions required for a phonon to be observable in Ramanspectroscopy. It determines which components of the Raman tensor $\boldsymbol{R}$ are zero and which are non-zero. For crystals with high symmetry many transition matrix elements are zero and thus the transition is forbidden. This results in selection rules, i.e. for a specific polarisation ($\boldsymbol{E_i}$;$\boldsymbol{E_s}$) Raman lines or phonon modes depend on crystal symmetry. More generally, these selection rules are the result of a treatment of crystal symmetry based on group-theory [20].

The dielectric susceptibility tensor, introduced in paragraph 3.1 and 3.2, is proportional to the Raman tensor $\boldsymbol{R}$ mentioned above. This tensor is associated with the Raman intensity by the relation [21]:

$$I \propto \left| \vec{E}_s \cdot \vec{\vec{R}} \cdot \vec{E}_i \right| \qquad (4.12)$$

Thus the Raman tensor determines which combinations of polarisation of the incident and scattered light, leads to a non-vanishing intensity.

Before we continue, a deeper understanding concerning the electron-phonon interaction is required. The influence of a phonon on the electronic band structure is through the lattice vibration itself. A time-modulated potential due to the lattice deformation arises [19]. This kind of interaction is called deformation potential (DP) scattering and applies for LO and TO modes. However, for (partly) polar or ionic crystals, such as III/V semiconductors, there exists an additional interaction, the so-called Fröhlich mechanism [23]. It arises for the LO mode, as treated in paragraph 3.3, because of the macroscopic electric field associated with it. This electric field may also interact with the electron system. For our purposes the DP scattering is the most important, since it generally yields the highest Raman intensity.

Using a group-theoretical treatment [20] the Raman tensors can be derived for all types of Bravais lattices. For III/V semiconductors the $\bar{4}3m$ symmetry applies. In the main crystal axis system, where x = [100], y= [010] and z = [001], the Raman tensors only have off-diagonal non-zero elements and become [19]:

$$\vec{\vec{R}}(x)=\begin{pmatrix}0 & 0 & 0\\ 0 & 0 & a\\ 0 & a & 0\end{pmatrix} \quad \vec{\vec{R}}(y)=\begin{pmatrix}0 & 0 & a\\ 0 & 0 & 0\\ a & 0 & 0\end{pmatrix} \quad \vec{\vec{R}}(z)=\begin{pmatrix}0 & a & 0\\ a & 0 & 0\\ 0 & 0 & 0\end{pmatrix} \qquad (4.13)$$

where x,y and z represent the direction of the lattice deformation induced by the phonon. These Raman tensors are valid only for DP scattering of phonons from the centre of the Brillouin zone, or Γ-point where $\boldsymbol{q}$ equals zero.

Most samples are grown in the [100] direction or deviate no more than 2 degrees from it. Therefore we discuss the back scattering geometry at a (100) surface, which was used in the experiments. Consider a photon travelling in the x-direction and impinging on the crystal, normal to the surface plane (100), where it is inelasticly scattered. The momentum conservation requires that the scattered light propagates in the direction opposite to the incident light. In addition, the transversality of light waves requires that the polarisation must be in the y,z plane. Thus the only Raman tensor elements which can contribute to Raman scattering are R^{yy}, R^{zy}, R^{yz}, and R^{zz}. However, the possibilities are reduced by crystal symmetry, represented by the

Table 4.1: Raman scattering configurations for the LO and the TO phonon for Deformation-Potential (DP) and Fröhlich (F) interaction.

Plane	E_i	E_s	LO	TO
100	010	001	DP	-
	010	010	F	-
	001	001	F	-
	011	011	DP, F	-
	011	01-1	-	-
110	1-10	1-10	F	DP
	1-10	001	-	DP
	0 01	001	F	-
111	1-10	1-10	DP, F	DP
	1-10	11-2	-	DP
	11-2	11-2	DP, F	DP

Raman tensors in equation (4.13). The components mentioned above only occur in Raman tensor $\boldsymbol{R}(x)$, which we associated with a lattice deformation in the x-direction. The propagation direction of the phonon is imposed by the momentum conservation law (equation 4.2) and is in the x-direction. Since this direction and that of the lattice deformation are the same, we deal with a LO phonon. Thus we conclude that for back scattering at a (100) surface only the LO phonon is symmetry allowed.

The discussion above is valid for DP scattering, but does not apply for the Fröhlich interaction mentioned before. This interaction only occurs for finite q and can only be observed when the energy of the incident light (almost) matches the energy of a transition in the crystal. The Raman tensor for Fröhlich interaction only has diagonal elements, thus the incident and scattered light have the same polarisation. Generally, the Fröhlich interaction is extremely small for scattering at the Γ-point [19]. Table 4.1 shows an overview of the different allowed polarisation's and scattering mechanisms for the (100), (010) and (001) crystal planes.

Since there are many configurations in which Raman measurements can be performed we use a convenient method to define the experimental configuration, the so-called PORTO-notation: $\boldsymbol{k}_i(\boldsymbol{E}_i;\boldsymbol{E}_s)\boldsymbol{k}_s$. In this work we use the configuration given by 100 (010;001) -100, to which we will also refer as the off-diagonal configuration. The 100 (001;001)-100 will be referred to as the diagonal configuration.

In our example we assumed back scattering on a (100) crystal plane. For the analysis of (110) or (111) planes we can show that in back scattering measurements at a (110) plane only TO phonons should be Raman active, while at a (111) plane both the LO and the TO phonon are allowed to appear.

The selection rules above only apply for the exact back scattering geometry for a perfect crystal, but can be affected when the conditions for back scattering are not exactly full filled or the crystal structure suffers from defects, impurities or other features which destroy the translation invariance. This results in the violation of momentum conservation and thus in the appearance of phonons with finite q value. Further, part of the lattice symmetry is broken, the selection rules deviate, and other phonon modes, such as a TO phonon, become observable. In the case that back scattering conditions are satisfied, generally the ratio between the LO and the TO phonon mode is directly related to the crystallographic quality of the structure. Also the shape and the width of the Raman peaks are an indication for the crystal quality. When the momentum conservation law is violated, optical phonons with larger q and thus smaller frequency occur. This can also be seen in figure 3.4, optical phonons with larger q have a smaller frequency. Thus the Raman peaks in the spectra broaden asymmetrically to the low energy side of the peak. For mixed compound crystals (section 3.4) an additional broadening occurs. The atoms of the group which contains two types, are randomly distributed and thus the translation invariance of the crystal lattice is violated.

For the investigation of interfaces, symmetry considerations are especially important since they give rise to a reduced symmetry and thus the violation of selection rules.

4.4 Penetration Depth

In this section we give a brief description of the penetration depth of light in a crystal. The penetration depth of light in a crystal can be varied by changing the laser frequency. This is a result of the dependence of the penetration depth on the light absorption, due to energetic transitions in the crystal (like the bandgap). Hence the penetration depth is frequency and material dependent. When the energy of the impinging light increases, the penetration depth decreases. This is due to the larger photon energies, which are more likely to create an excitation, because also larger energy transitions become

involved. Especially at specific electronic transitions, like the bandgap E_o, a steep decrease of the penetration depth has to be expected.

We define the penetration-depth d_p, as the depth at which the intensity of the incident light is decreased to 1/e-th of the initial intensity I_o, i.e.:

$$I(d) = I_o \cdot e^{\frac{-2d}{d_p}} \qquad (4.14)$$

where $I(d)$ is the light intensity at depth d. Because the light we want to observe in spectroscopy has to penetrate the crystal and subsequently leave it, a factor 2 is included in equation (4.14).

As mentioned above, the penetration depth is dependent on the frequency of the incident light, i.e. the laserline. This gives us the possibility to investigate layers at different depths. The high energy (violet/green) laserlines are suited for a surface analysis because of their limited penetration depth, while the long wavelength laserlines (red) allow examination of the deeper parts of the structure. Some material can even be transparent for long wavelengths. In Figure 4.2 the penetration depth of GaAs, InAs and InP is depicted as a function of the wavenumber of the incident light. The laserline at 20492 cm^{-1} is represented by a dotted line, because with this line all Raman spectra were obtained.

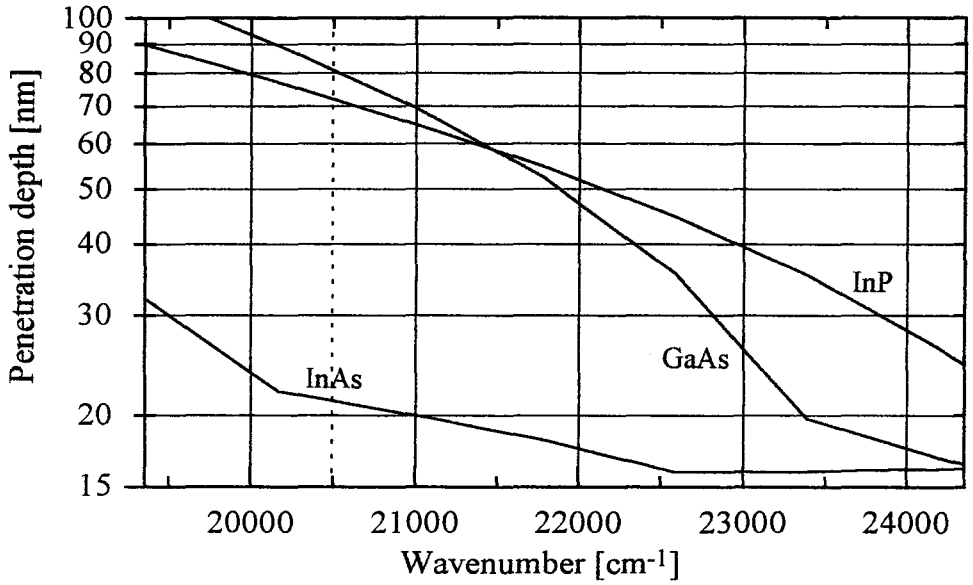

Figure 4.2: Dependence of the penetration depth (defined in equation 4.14) on the wavenumber of the incident light for the materials InAs, InP and GaAs.

4.5 Raman Spectroscopy on Superlattices

So far we only discussed Raman spectroscopy on bulk material. However, in this work we also examine superlattices (SL). These consist of a periodic sequence of two different semiconductor materials along the growth direction. The physical properties of these structures with respect to phonons differ substantially from that of bulk material. In SL new phonon-modes appear, which give rise to new features in Raman spectra which can give additional information on the layer structure. From the variety of new phenomena including folded-acoustical-phonons (FAPs), interface phonons and confined optical phonons, only the latter will be discussed here. For the other types we refer to 'The Physics of Phonons' by Srivastava [24].

Consider a SL consisting of material A and material B, as shown at the right side in Figure 4.3. The propagation of an optical phonon in a layer of material A or B strongly depends on the dispersion relation, i.e. the material. This implies that in general for a lot of combinations of the materials A, B forming a superlattice, the optical phonon frequencies do not exhibit any overlap, as depicted in Figure 4.3. Thus the optical phonons can not propagate from material A to material B, because in material B no eigenmode exists at the eigenfrequency belonging to the phonon in material A. The optical modes are confined to layers of material A or B respectively and are therefore called confined-optical-phonons. They show a behaviour analogue to a standing wave or an electron in a quantum well. Likewise, only an integer of

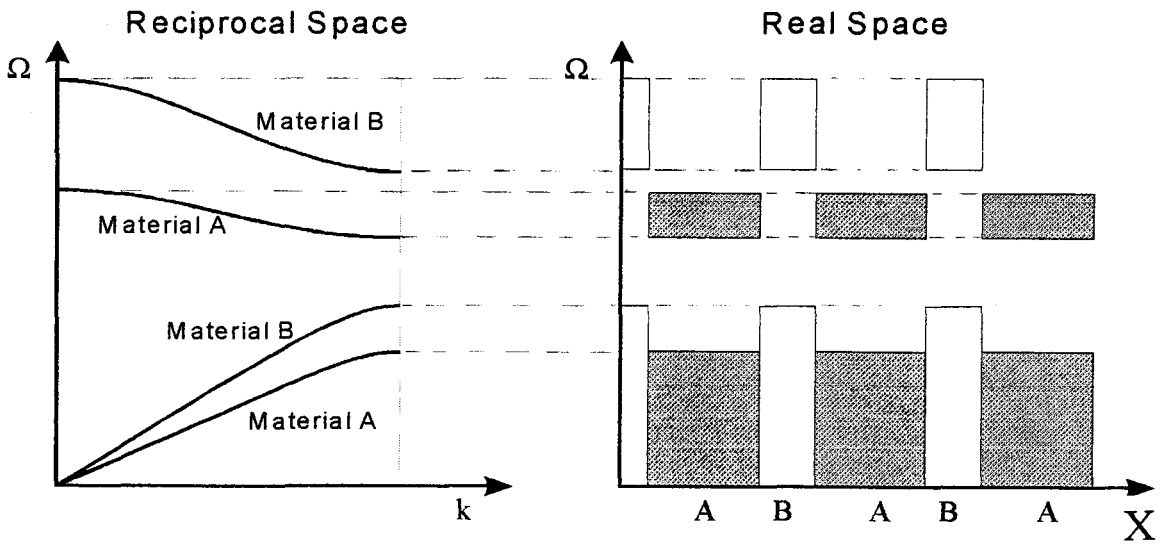

Figure 4.3 (left) The dispersion curves for two materials in reciprocal space for which the optical modes do not overlap, and (right) the structure of the superlattice in real space.

half wavelengths is allowed for the phonon in the layer, since the displacement at the boundaries of the layer should be zero: $u(d) = u(0) = 0$. This results in an expression for the wavenumber q of the phonons:

$$q = n \cdot \frac{\pi}{d} \qquad n = 1,2,3,... \qquad (4.15)$$

where n is an integer and d is the thickness of the layer. This equation means that we can expect multiple phonon modes in the layer. Therefore, in the Raman spectrum a series of peaks may be observed, because their frequencies are determined by the dispersion curves, which means that peaks with higher index n will appear at a slightly lower frequency (figure 3.4).

As a result of the selection rules, we can distinguish phonon modes with even or with odd symmetry. Modes with odd index n have an even symmetry, while modes with an even index n have an odd symmetry. This apparent contradiction can be explained. In Raman spectroscopy only phonons with even symmetry are allowed for deformation potential scattering in crystals with a centre of inversion. In a SL the centre of symmetry is the middle of a layer. Therefore, only phonons with odd n (even functions in space) are allowed in the off-diagonal configuration, i.e. the (100) backscattering geometry. However, III/V semiconductors are partly polar and thus also the Fröhlich interaction is present. This means that the confined modes with odd symmetry and thus even index n, are observable in the diagonal configuration, i.e. when the incident light is polarised along a main crystal axis, for instance [001]. The selection rules enable us to determine whether Raman peaks originate from confined phonons or not. Another indication for confined phonons is the distinct frequency shift between the frequency of the bulk LO phonon and the phonon of the first confined mode (LO_1), which appears at a slightly lower frequency due to a decreasing dispersion curve for higher q values.

The phonons in the SL structures investigated in this work, show no confined behaviour. This is due to the thickness of the layers, which is too large and therefore results in a non-observable frequency shift of the confined phonons, i.e. the q-vectors of the phonons are limited to an extreme small region around the Brillouin zone centre. The intensity of the confined modes decreases rapidly as the order n increases. Hence often the shift of the LO phonon is the only indication of confinement.

A necessary condition for confined phonons to exist is that the interfaces are sharp or abrupt. Meaning that no coupling between the lattice vibrations of material A and B is possible. Thus when confined phonons are observable the interfaces between the constituent layers of materials A and B of the SL are abrupt.

5. Raman experimental Set-up

In this chapter we discuss the experimental set-up required for Raman spectroscopy. The description presented in this chapter is based on the work of Dipl.-Phys. M. Pohlmann [24], Dipl.-Phys. J. Tümmler [25] and Prof. Dr. J. Geurts [19]. All Raman measurements presented in this work were performed using the Raman set-up at the RWTH in Achen.

One of the main components we need to observe Raman light is a monochromatic lightsource. The impinging light must have a precisely defined energy, because we observe a shift with respect to this energy, the so-called Raman shift. The lightsource should also have multiple wavelengths distributed over a broad spectral region (400 to 900 nm), since we want to take full advantage of the possibilities of the variation of the penetration depth (section 4.4) in the various semiconductor materials. For this purpose the combination of two gas-lasers is used, namely an Ar^+ and a Kr^+ gas-laser. These lasers and the light trajectory between the laser and the spectrometer, are discussed in section 5.1.

Another requirement for the observation of Raman active transitions, is a high stray light suppression. We must prevent the Rayleigh and diffuse reflected light from entering the detection system. Therefore, at least a double grating monochromator system is mandatory. Because the Raman light is very weak in intensity, we also need an extremely sensitive detector. In general this is a Photo-Multiplier (PM) or an Optical-Multichannel-Analyser (OMA). The entire detection system, i.e. monochromator and detectors, is discussed in section 5.2.

5.1 Lightsource and Light Trajectory

A monochromatic lightsource is not the only requirement on the laser system to perform Raman measurements. Additionally, it must have multiple wavelengths and give a light beam with high intensity, since Raman scattering is a second order and thus weak effect. In the Raman set-up we use, all three criteria are satisfied by use of a Ar^+ and a Kr^+ gas-laser, of the manufacturer Coherent. The combination of the Ar and the Kr-laser gives a discrete set of laser lines ranging from the violet via the green to the near-infra-red (NIR).

Table 5.1: Laserlines of the Ar^+- and the Kr^+-gaslasers with their physical properties.

gas-laser	k [cm^{-1}]	λ [nm]	E [eV]	Power [W]	Colour
Argon	19436	514.5	2.41	1.7	green
	19932	501.7	2.47	0.3	dark green
	20141	496.5	2.50	0.5	blue-green
	20492	488.0	2.54	1.3	turqois
	20986	476.5	2.60	0.5	bright-blue
	21115	472.7	2.62	0.1	blue
	21448	465.8	2.66	0.07	blue
	21839	457.9	2.71	0.3	dark-blue
Krypton	14784	676.4	1.83	0.12	red
	15454	647.1	1.92	0.5	red
	24207	413.1	3.00	0.15	violet
	24586	406.7	3.05	0.15	violet

The different emission lines with their constituent power outputs are given in Table 5.1, for both lasers. Note that the short wavelength lines of the Kr-laser have a low intensity and thus are of limited practical use. A specific emission line from the plasma is enhanced using selective amplification by means of a prism positioned between the resonators. For Raman spectroscopy the laser is only operated in this mode, the so-called single-line-mode. Additionally, the Ar-laser is equipped with light-mode operation for the emission lines at 19436 cm^{-1} and 20492 cm^{-1}, which means that fluctuations in the light output are measured and compensated for, by adapting the electric current. This feedback control results in a constant light output. The standard line used for the measurements in this work is the emission line at 20492 cm^{-1}. This line combines a large power output of maximum 1.3 Watt, with a reasonable penetration depth, approximately 80 nm (section 4.4), and the convenience of light-mode operation. The light beam is 1.5 mm in diameter and has a divergence of 0.25 mrad. The line width of the laserline is $\Delta\lambda = 8{,}83 \cdot 10^{-3}$ nm, specified in the manual for a wavelength of $\lambda = 514.5$ nm (19436 cm^{-1}).

The laser light, which emerges from the laser, is guided through a special prism, as depicted in Figure 5.1. This prism is used to filter out the emission lines which are not resonant enhanced (plasma lines) and consist of three individual prisms. The advantage of this combined prism compared to a normal (single) prism is that the light beam is approximately diffracted back to its initial direction. Thus when changing the laser line, only little re-justification is necessary. Light with a wavelength of $\lambda = 587{,}6$ nm does not experience a deviation from the initial angle of direction. Further, such a

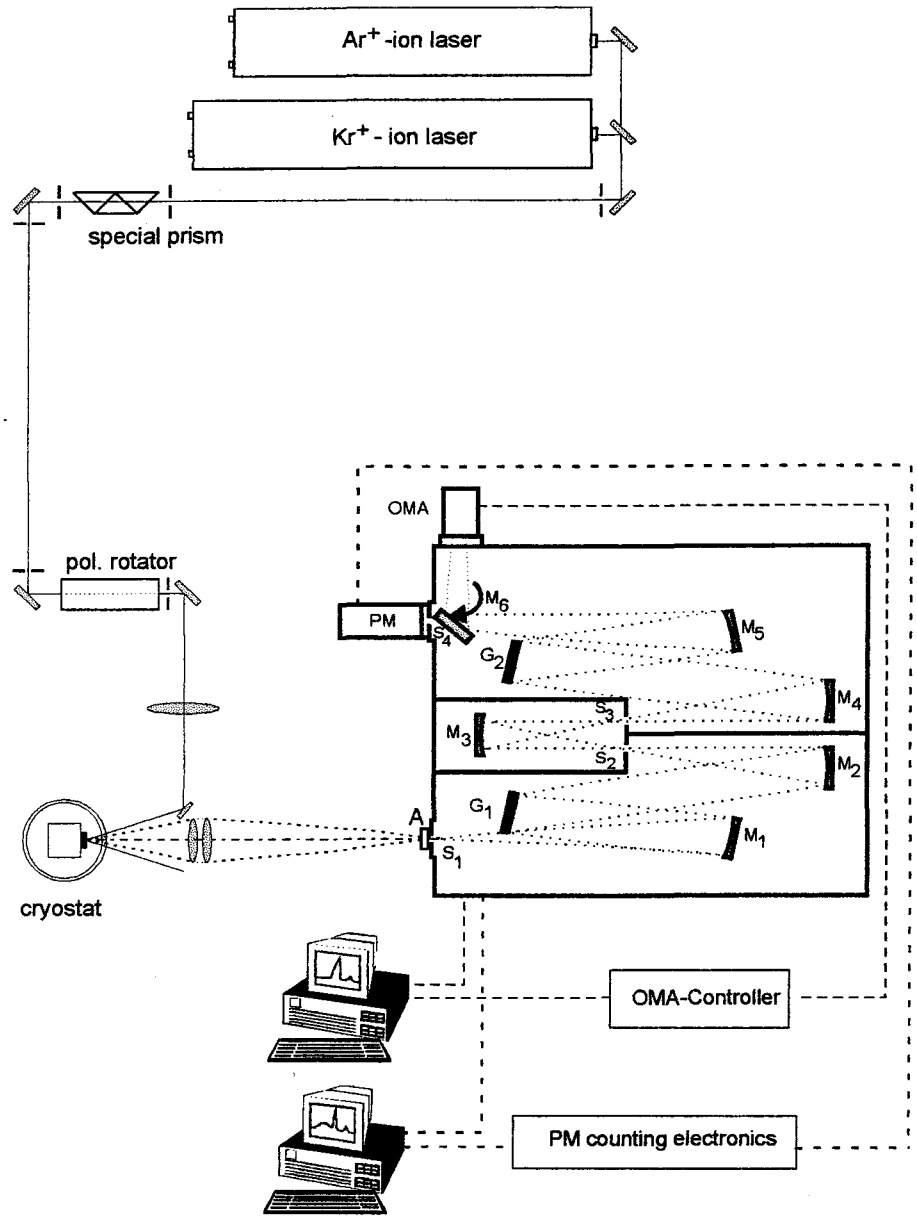

Figure 5.1: Basic overview of the Raman set-up. All symbols and components are discussed in the text.

prism gives a higher dispersion than a 'normal' prism, resulting in a better separation of the preferred laser line from the superfluous plasma lines. However, the longer optical path and the two additional diffraction planes lead to an attenuation of the light intensity. Therefore, the prism can not be used for the weaker laser lines.

In order to complete the removal of the redundant plasma lines from the light beam, the light is guided through two apertures ±1,2 m separated from each other. In this way the plasma lines, which were spatially split up by the

prism, are obstructed. Meanwhile, a horizontal path of the beam is accomplished.

In section 4.3 the importance of symmetry and the associated selection rules has been pointed out. To be able to manipulate the polarisation of the incident light and thus use the selection rules to advantage, a polarisation-rotator is used. The light from the laser is vertically polarised, according to manufacturer specification. By turning the polarisation-rotator around its longitudinal axis, we can continuously adjust the angle of the polarisation and thus the ratio between the vertical and horizontal components. Generally, this polarisation-rotator is used to obtain purely horizontally or vertically polarised light. Next, the light is reflected via mirrors and directed through a lens. The laser beam can be focused by varying the distance between the lens and the sample. To obtain different focus diameters a set of lenses is available. All measurements in this work were performed using a lens with a focal length of 10 cm. Then the focus diameter is approximately 50 μm. If a smaller focus is necessary, we can use a micro-objective which makes spatially resolved Raman spectroscopy possible, with a focus diameter down to 2 μm. There exists a lower limit for this diameter due to the associated high excitation density which can result in local heating of the sample and destroy it. Thus a low power output of the laser is necessary. However, this leads to a weak Raman signal. To be able to use higher power outputs anyway we should use a cylindrical instead of a spherical lens, which gives a line-focus. Comparison of spectra recorded by either a point- or a line-focus, gives a quick indication of the lateral homogeneity of the sample.

For most III/V semiconductors the zinc-blende structure applies (section 1.2). For a (100) substrate, which is basically a stack of (100) planes, this leads to cleave-planes in the [011] and the [01-1] directions. These cleave-planes enable an easy positioning of the sample with respect to the polarisations of the incident light. For low temperature measurements at 80 K, the samples are fixed to a copper-block which is in thermal contact with a reservoir containing liquid nitrogen, which is thermally isolated from the environment by evacuation with a turbomolecular pump. The entire cryostat can be precisely moved in x, y and z direction, allowing a very accurate justification of the sample with respect to the incident light.

The scattered light from the sample consists of the Raman and the diffuse reflected light and is projected on the entrance slit of the monochromator

with a standard 50 mm photo-objective. The direct reflection of the laser beam is obstructed. The distance between the photo-objective and the sample should be kept small in order to collect the majority of the scattered light (large collection angle). In front of the entrance slit of the monochromator, a polarisator (analyser) is present to assure that only the intensity of the selected polarisation is measured. The combination of the analyser and the polarisation-rotator mentioned earlier, allow a separate analysis of the individual components of the Raman tensor and thus enables us to take full advantage of the selection rules.

5.2 Detection System

The detection system consists of two main parts, namely a spectrometer and a light detector. Either will be discussed separately.

The light intensity from the Raman scattering process is extremely low compared to the intensity of the diffuse reflection of the laser beam. Therefore, a double grating monochromator is used, the Model 1403 supplied by the firm Spex. The monochromator is operated in the so-called Czerny-Turner configuration, which yields a additive dispersion, meaning that grating G_1 diffracts the light in the same direction as grating G_2. In Figure 5.2 the light-trajectory inside the monochromator is shown. Light entering the monochromator through entrance slit S_1, reflects at mirror M_1 and is diffracted at grating G_1. Subsequently, the mirrors M_2 and M_3 direct the light

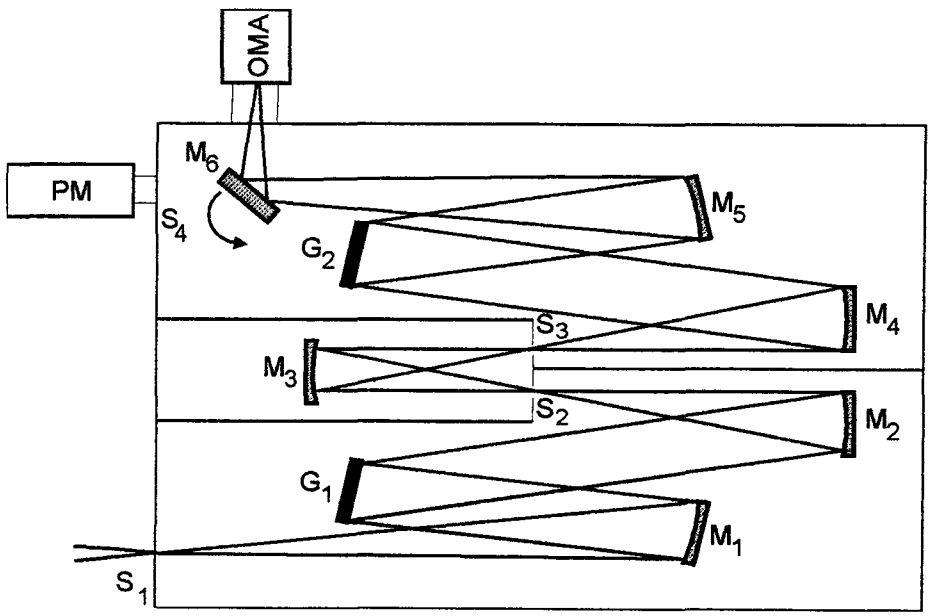

Figure 5.2: Detail of the light trajectory inside the double grating monochromator. The symbols are explained in the text.

through adjustable slits S_2 and S_3, which are necessary for stray light suppression. Via mirror M_4 the light impinges on the second grating G_2, where it is diffracted again. The grating is rotated by a step-motor which is controlled by a personal computer. By rotating this grating a wide spectral range between 11000 cm^{-1} and 27000 cm^{-1} is covered. Comparison with the available laser lines shows that this range fully meets the requirements. The holographic gratings G_1 and G_2 are both 10 cm, with a linenumber of 1800 mm^{-1}. They are operated in the first order diffraction configuration. For light with a wavenumber of 20492 cm^{-1} (λ = 488 nm), the spectral resolution is 0.06 cm^{-1}. Nevertheless, the resolution is mainly determined by the width of the entrance slit S_1. A smaller slit gives an increased resolution, but a reduced Raman intensity reaching the detector. All measurements presented in this work were performed with a slit width of 150 µm, which gives a resolution of 1 cm^{-1} for the laser line with wavenumber 20492 cm^{-1}.

Dependent on the position of mirror M_6, light can be detected with a photomultiplier (PM) or an Optical-Multichannel-Analyser (OMA). When using the PM only a small part of the spectral range is taken into account. Hence the slits S_2 and S_3 are only a little wider than the entrance slit S_1. This results in a very high stray light suppression. Consequently, the measurements can be performed extremely close to the laser line. The spectral range of interest can be selected by rotating both gratings. Measuring successive spectral ranges results in a scan of a particular spectral region. The noise in the spectra can be reduced by performing several measurements and averaging them. Likewise the main disadvantage of the PM becomes clear, as the time to obtain a satisfactory measurement is long.

In contrast to the PM, the OMA is able to measure the intensity of the light in a spectral region of approximately 200 cm^{-1} at once. Likewise, the positions of the gratings are not changed. This method to obtain spectra is much faster compared to the method with the PM. However, because the OMA records a wide spectral range during one exposure, the slits S_2 and S_3 have to be fully opened. As a result the stray light suppression becomes much smaller. Therefore, measurements using the OMA can only be performed at least 150 cm^{-1} away from the laser line. Moreover, the samples should have a very low level of diffuse reflection. This last condition is fulfilled for high quality epitaxial layers, as present in the structures studied in this work.

The OMA detector consists of 1024 Si-diodes, each 25 µm broad. Before each measurement, all diodes are charged till they have a potential of +5 V. Due to the impinging photons this potential drops. At the end of the exposure time, the remaining potential is read out using a 14 bit analogue-digital-converter. Hence, the maximum integral intensity is $2^{14} \approx 16000$ counts per measurement. Usually, the measurements take 2 minutes each, yielding a maximum intensity of 135 counts per second (cps). To reduce the 'white' noise, several spectra are measured and added up. The resulting spectrum is divided by the total measuring time.

The OMA detector is cooled by a Peltier element in order to reduce the thermal noise. The element accomplishes a temperature gradient of 25 °C between the 'hot' side and the 'cold' side. The 'hot' side of the element is cooled by an external cooling circuit, which keeps the temperature steady at -10 °C. Consequently, the 'cold' side of the element has a temperature of -35 °C, which reduces the noise significantly. A flow of technical nitrogen is used instead of environmental air to prevent the condensation of water and the formation of ice on the detector.

6. Results and Discussion

We will now discuss the results of the Raman measurements on the various samples. In section 6.1 we start with the MBE samples, bulk $In_{1-x}Al_xAs$ layers on InP, for which we described the interface layer formation, due to the annealing process, described in section 2.2. Next, in section 6.2 we consider the Raman spectra of InAs / InP superlattice structures grown by CBE on various substrate orientations. Finally, we describe the Raman measurements on $In_{1-x}Ga_xAs$ / InP superlattices also grown by CBE, and we discuss the differences in the spectra due to different misorientations and different growth interrupt sequences.

6.1 MBE samples: Bulk $In_{1-x}Al_xAs$ on InP

In section 2.2 we have described the formation of InAs interface layers due to the thermal annealing process of an InP substrate. Before we discuss the Raman spectra of the different samples, we start with the explanation of the various structures in the Raman spectrum. In Figure 6.1 a Raman spectrum of sample W697, with an annealing time of 4 min. is shown. The peak at 349 cm^{-1} in the Figure 6.1b corresponds to the InP LO peak. Considering the resolution (1 cm^{-1}), this is in good agreement with the value 349.5 cm^{-1} known from literature [26]. The small structure at 306 cm^{-1} corresponds to the InP TO mode, which is forbidden in the (100) back scattering configuration and can indicate degradation of the crystallographic quality of the InP. This small but non-vanishing intensity can also be induced by an imperfect (100) back scattering geometry. However, then for all materials for which the LO mode is observed, the TO modes should also appear. Since these TO modes are not observed, the InP TO will most probably be due to a degraded crystallographic quality.

It is known that $In_{1-x}Al_xAs$ exhibits two-mode behaviour [27], as can also be concluded from equation (3.28). The peak at 371 cm^{-1} in Figure 6.1b, is the AlAs-like LO mode associated with the ternary compound. The peak is broad compared to the peak of the InP LO mode. The broadening can be induced by different causes, namely:
i) a gradient in the composition of the layer, which also gives rise to strain.
ii) disorder in the layer. For instance alloy clustering, which affects the translation invariance and thus leads to violation of the selection rules. This results finite q values and thus (via the phonon dispersion, Figure 3.4) to op-

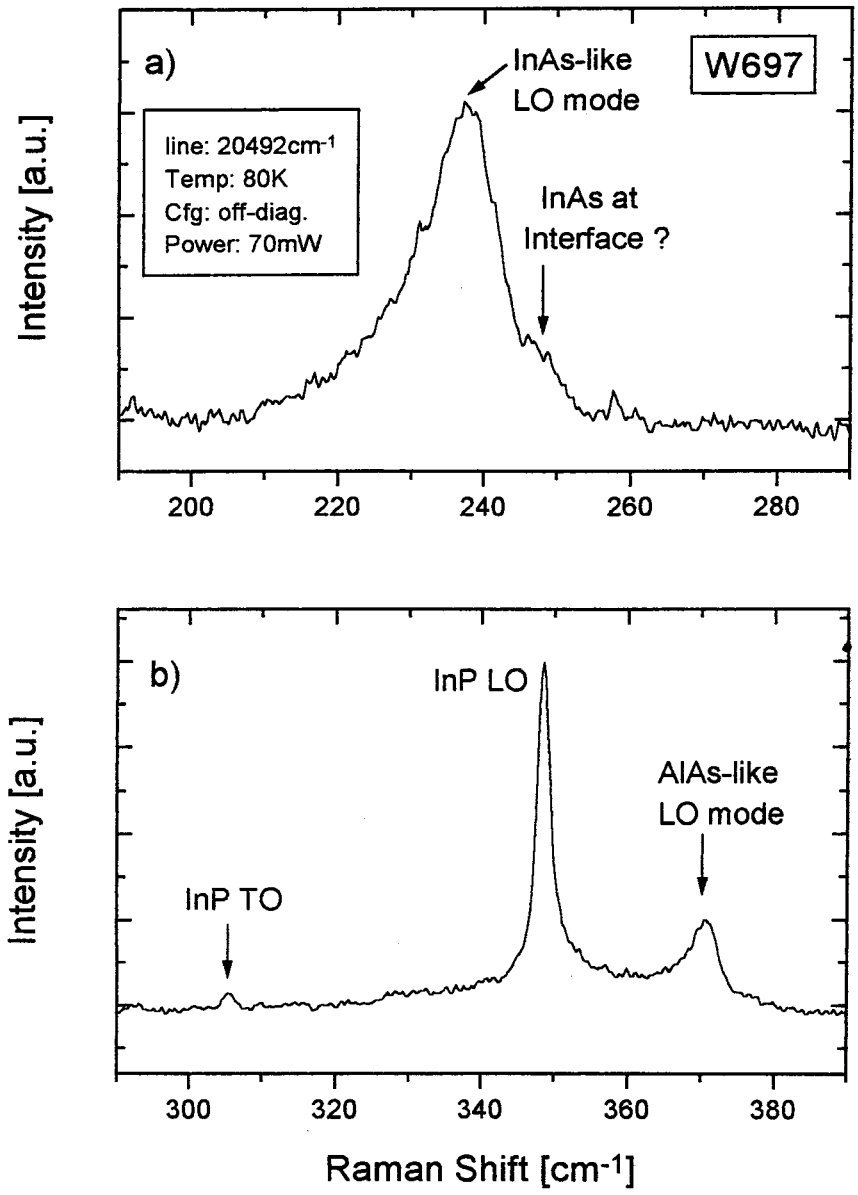

Figure 6.1a Raman spectrum of the As-region of MBE sample W697 and **6.1b** the spectrum of the region around the InP LO peak.

tical phonon modes with lower energy, which gives rise to a peak that is asymmetrically broadened at the low energy side.

In Figure 6.1a there is a peak at 239 cm^{-1}, which is associated with the InAs-like LO mode of the ternary $In_{1-x}Al_xAs$. This peak is also quite broad compared to the peak of the InP LO mode. The same arguments for the broadening, mentioned above for the AlAs-like mode apply here. We ob-

serve some additional structure at the right of the main InAs peak, namely at 246 cm^{-1}. We associate this structure with strained InAs at the interface between $In_{1-x}Al_xAs$ and InP.

To investigate the influence of the annealing time, we have normalised the Raman spectra of the samples, as shown in Figure 6.2. Only the spectra of the sample W677, W696 and W697 are shown, because the spectra of W694 and W695 coincide with the spectrum of W697. The spectra in Figure 6.2a are normalised to the InAs-like peak, while the spectra in Figure 6.2b are normalised to the AlAs-like peak. In this way we are able to compare the spectra of the various samples. We do not normalise on the InP LO peak, because the thickness of the $In_{1-x}Al_xAs$ layer after etching is different for each sample. Clearly, from Figure 6.2b there is no obvious distinction between the spectra. The InP LO peak is positioned at 349 cm^{-1}, which is in agreement with the value known from literature 349.5 cm^{-1}. The AlAs-like LO mode is observed at 371 cm^{-1} for W696 as well as W697, and at 372 cm^{-1} for W677. The shift is due to a lower indium concentration in W677, which is in agreement with XRD measurements and the results of a study on the mode behaviour of $In_xAl_{1-x}As$ [27]. Note that the AlAs-like peaks are asymmetrically broadened at the low energy side.

Next to the AlAs-like LO mode, we also observe an InAs-like LO peak, as shown in Figure 6.2a. This peak dominates the entire As region. It is positioned at 238 cm^{-1} for the samples W696 and W697, and at 236 cm^{-1} for sample W677. In our opinion the shift is caused by a lower indium concentration in sample W677 ($x = 0.502$) compared to W696 and W697 ($x \approx 0.476$), which gives rise to a red-shift of the InAs-like LO mode. This is in agreement with literature.

Around 246 cm^{-1} an additional structure is almost resolved. As mentioned earlier, this broad peak is associated with strained InAs at the interface. For W696 no such peak is observed, due to the thick $In_{1-x}Al_xAs$ layer. Because the InP LO phonon is not observed, no structures related to the InAs interface are observed either. This is a direct indication that the broad structure around 246 cm^{-1} in the spectra of the samples W677 and W697, originates from the InAs interface. Nevertheless, the structure is not entirely resolved and thus does not lead to additional information on the interface.

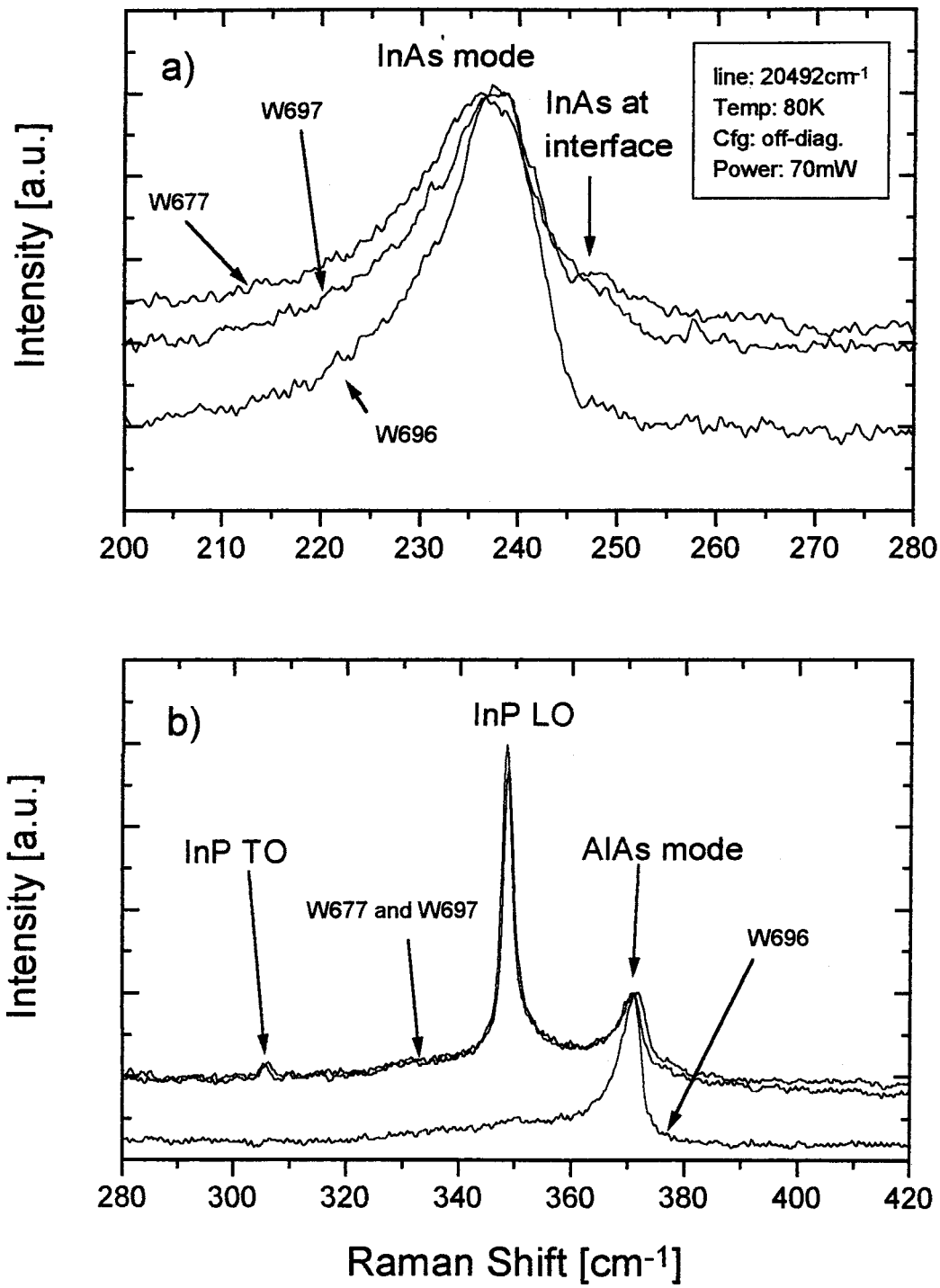

Figure 6.2a Raman spectra of the samples W677, W696 and W697 normalised on the InAs-like LO peak, and **6.2b** the Raman spectra of the same samples normalised to the AlAs-like LO peak.

6.2 CBE Samples: InAs / InP Superlattices

In this section we discuss the influence of the various misorientations on the structures in Raman spectra, due to interface layers of approximately 1 ML formed by substitution resulting from a GIS (section 2.2). The Raman spectra of the sample series C382-1/2/4/5 is depicted in Figure 6.3. We will now try to explain the various peaks in the spectra, starting with the InP LO peak.

For all spectra the peak is positioned at 349 cm^{-1}, which is in agreement with the value known from literature [26], 349.5 cm^{-1}. The InAs peak should appear around 240 cm^{-1} but was not observed, probably due to a low concentration of the InAs in the layer structure. The InP LO peaks of the samples C382-2/4/5 are very broad (Full Width Half at Maximum > 10 cm^{-1}) compared to the InP LO peak of C382-1 (FWHM ≈ 6 cm^{-1}). This indicates a degraded crystallographic structure of the InP layers in these samples.

Left from the InP LO peak, at 345 cm^{-1}, another peak is observable for the samples C382-2/4/5. This peak can originate from a confined mode with

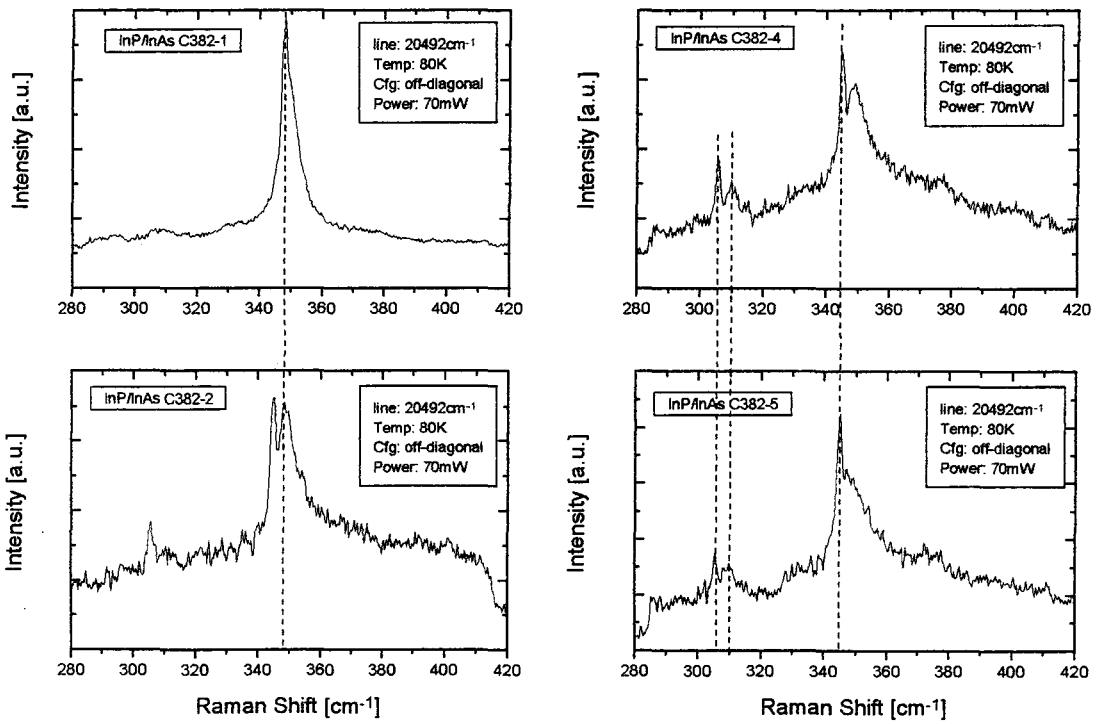

Figure 6.3: Raman spectra of the CBE InAs/InP superlattice structures, recorded in the off-diagonal configuration. The various peaks are discussed in the text.

index 3 in the InP (section 4.5), or a surface mode of the InP. A surface mode consists of a phonon which propagates along the surface of the sample. In order to determine whether this peak is associated with a confined mode or a surface mode, we measured a spectrum in the diagonal configuration (the incident and the scattered light have the same polarisation), as shown in Figure 6.4. In the diagonal configuration the even index peaks of the confined mode are observable and the odd index peaks are not observable. However, in the spectrum the same peak at 345 cm^{-1} remains and no additional peaks are observed. Thus the peak does not originate from a confined mode. Consequently, we associate the peak with a surface mode, which is observable in diagonal and off-diagonal configuration. The surface mode is observed in the spectra of the samples C382-2/3/4/5, which corresponds to the same structure on an exact orientated substrate, 0.5° misorientation in (110), (111)A and (111)B direction respectively.

The InP TO-peak, which is symmetry forbidden in the (100) back scattering geometry, appears at 310 cm^{-1} in the samples c382-3/4/5. The value known from literature is 308.2 cm^{-1}. Thus considering the resolution (1 cm^{-1}), the InP TO peak is slightly shifted to a higher energy.

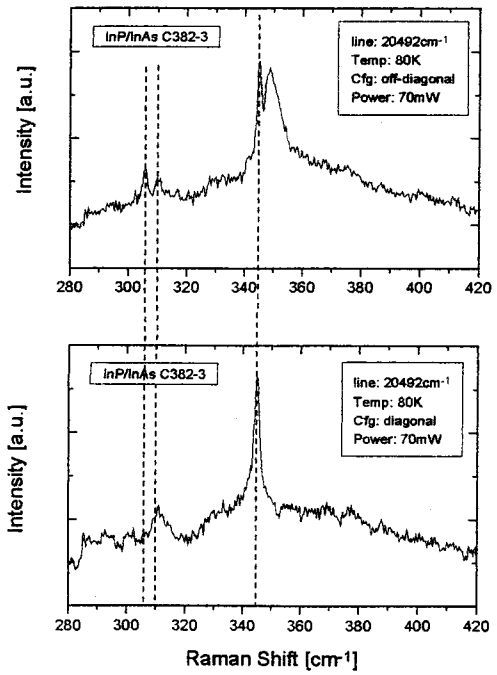

Figure 6.4: Raman spectra of the CBE InAs/InP superlattice C382-3. The upper graph presents the off-diagonal spectrum, while the lower graph contains the spectrum recorded in the diagonal configuration.

In the spectra of the samples C382-2/3/4/5 in Figure 6.3, an additional peak is observed at 305 cm^{-1}, which obeys the selection rules like a LO phonon. This means that the extra peaks are allowed in the off-diagonal configuration (Figure 6.4a) and forbidden in the diagonal configuration (Figure 6.4b). These peaks could originate from interface modes (IFM) which give rise to interface phonons. These are phonons which propagate along the interface between two adjacent materials. They normally appear between the TO and the LO frequency [28]. Therefore, the peak at 310 cm^{-1}, which we assigned to the InP TO, could also be the IFM, while the peak at 305 cm^{-1} could be associated with the InP TO. The IFM would then be associated with an interface phonon of $InAs_xP_{1-x}$. However, when $InAs_xP_{1-x}$ is present at the interface we expect to observe an InP-like LO mode of the $InAs_xP_{1-x}$ in the region between 330 cm^{-1} and 340 cm^{-1}, since $InAs_xP_{1-x}$ exhibits two-mode behaviour, like most ternary compounds. A slight enhancement of the intensity is observed in the spectra of the samples C382-3/4/5. However, when the peak at 310 cm^{-1} originates from a IFM, this implies that the InP TO obeys the selection rules, which is not the case since it is forbidden in this configuration and thus should not be observable at all. This contradiction can not be explained.

6.3 CBE samples: $In_{1-x}Ga_xAs$ / InP superlattices

In order to investigate the interface layers and the crystallographic quality of $In_{1-x}Ga_xAs$ / InP superlattices on various substrate orientations and for different growth interrupt sequences, Raman measurements were performed on two series of samples, namely C385-1 to C382-5 (misorientation dependent) and C383-5 to C386-5 (GIS dependent). Because the Raman spectra of these samples are more complex than the Raman spectra discussed in the preceding paragraphs, we will first describe an example spectrum as shown in Figure 6.5 [24].

The entire spectrum is divided into two regions, the As-region and the P-region. We discuss the structures in these regions successively and we start with the P-region. Clearly observable is the peak at 349 cm^{-1}, which is assigned to the InP LO mode. The peak directly left from the InP LO is assigned to the surface mode of InP. When the crystallographic quality of the InP is high, then no or little intensity is expected for the InP TO at 308 cm^{-1}. We now continue with the description of the peaks in the As-region. The ternary $In_{1-x}Ga_xAs$ exhibits two mode behaviour [29], which

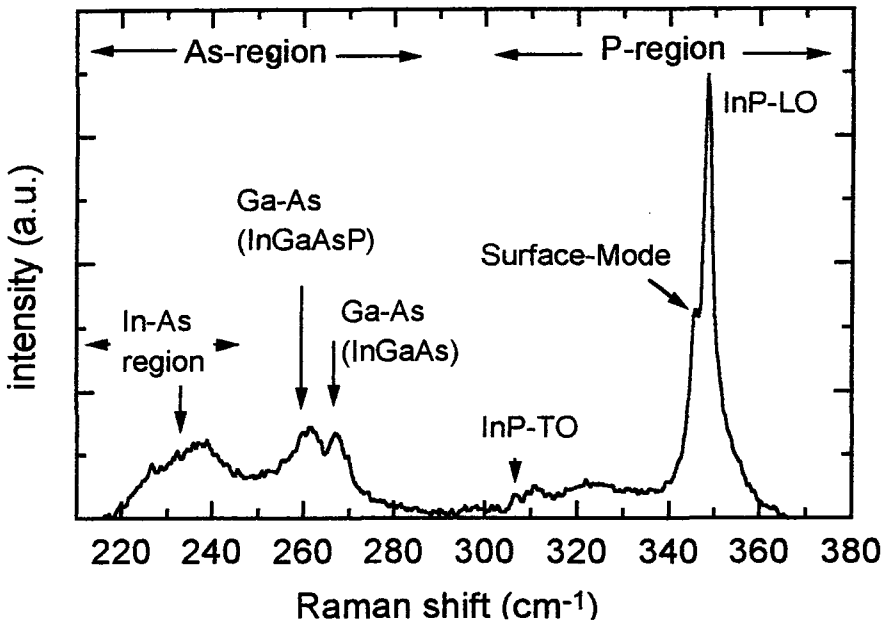

Figure 6.5: Example Raman spectrum of an $In_{1-x}Ga_xAs$ / InP superlattice. The entire spectrum is described in the text (Figure taken from [24]).

gives rise to a GaAs-like mode at 268 cm^{-1} and an InAs-like mode around 238 cm^{-1} (for lattice matched material). Left from the GaAs-like mode at 268 cm^{-1}, there is an another peak at 262 cm^{-1}, which is associated with the GaAs-like mode of the quartenary alloy $In_{1-x}Ga_xAs_yP_{1-y}$ [30]. The same quartenary alloy also gives rise to an InAs-like mode in the InAs region and an InP-like mode in the P-region. The InAs of the interfaces contributes also to the intensity in the InAs region. Further, the two modes of $InAs_xP_{1-x}$ give additional contributions in the InAs-region and the P-region (320 cm^{-1} to 340 cm^{-1}). This variety of InAs-like modes in the InAs-region gives rise to the broad structure in Figure 6.5.

In order to investigate the influence of the GIS (section 2.2) on the interface layer formation and the crystallographic quality, Raman spectra are recorded for the sample series C383-5 to C386-5. These samples are grown on substrates with 0.5° misorientation to (111)B and were selected because of the good surface morphology and the extremely low defect density [31]. The Raman spectra of the samples are depicted in Figure 6.6. For all spectra the InP LO peak is again positioned at 349 cm^{-1}. The InP TO is barely or not observed which indicates a high crystallographic quality. Further, in all spectra the GaAs-like mode is positioned at 270 cm^{-1}. This corresponds to the lattice matched position of the GaAs-like mode [32], which is in agreement with the composition obtained from XRD measurements. In the InAs

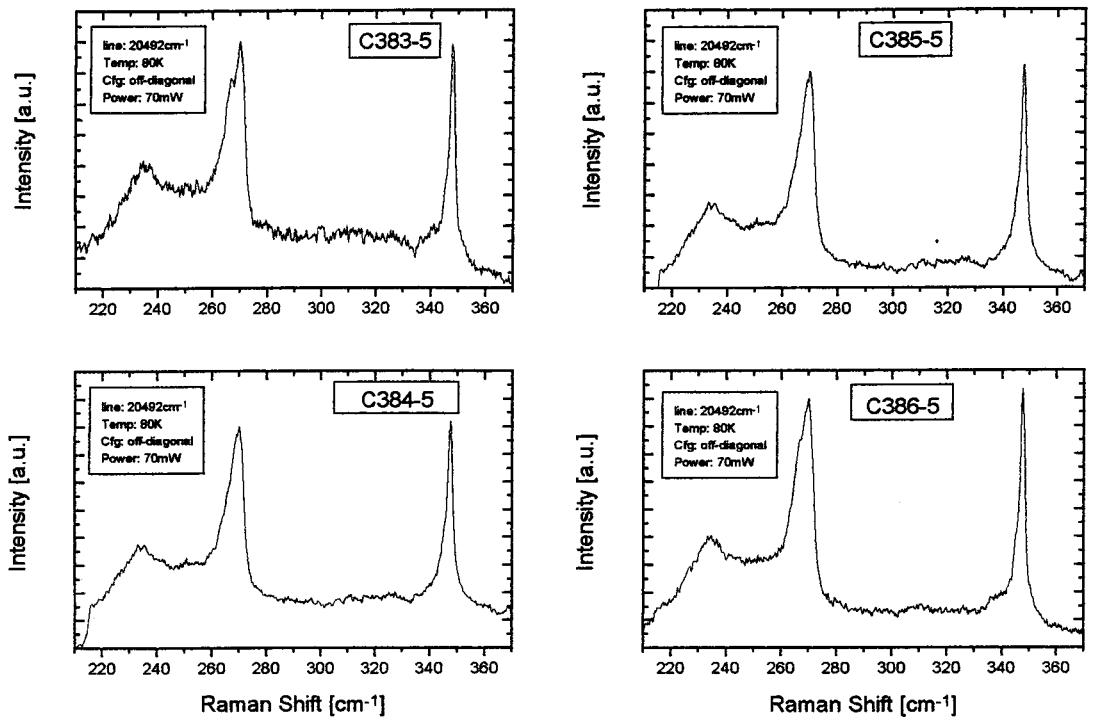

Figure 6.6: Raman spectra of samples with different growth interrupt sequences, but the same substrate misorientation, namely 0.5° to (111)B.

region no distinct peaks can be observed. There is only a broad structure present, from which we assign the middle to the position of the InAs-like mode of the $In_{1-x}Ga_xAs$. The overall differences between the spectra are minimal. However, for C383-5 and C386-5 the peak at 265 cm^{-1} seems to be more pronounced. This peak can be assigned to the GaAs-like quartenary mode, or to a GaAs-like mode of $In_{1-x}Ga_xAs$ which is slightly indium enhanced ($\approx$ 2%) somewhere in the structure. The first possibility would also give rise to a weak InP-like mode in the 330-340 cm^{-1} region and a weak InAs-like mode just below the InAs-like mode of $In_{1-x}Ga_xAs$. However, these modes are not observed. Thus the Raman spectra do not give a definitive conclusion. The GIS of C386-5 is (2,1,2,1) with extra indium, gallium and phosphorus offered at the interfaces. This can give rise to quartenary material. The GIS of C383-5 is (2,1,2,0) and thus one does not expect much quartenary material. Hence, in this sample the origin of the peak at 265 cm^{-1} is most likely an indium enhancement somewhere in the layer structure. Generally, we conclude that for this sample series there is not enough difference in the Raman spectra to draw any definitive conclusions on the influence of the GIS on the interfaces.

We will now discuss the effect of the substrate orientation on the Raman spectra of $In_{1-x}Ga_xAs$ / InP superlattices, namely the samples C385-1 to C385-5. These samples were selected because of the good result for the PL line width of sample C385-5 (FWHM 8.4 meV). The Raman spectra of these samples are shown in Figure 6.7 (next page). In all spectra the InP LO peak is positioned at 349 cm^{-1} and no InP TO is observable at 308 cm^{-1}, thus the InP has a high crystallographic quality. The peak of the GaAs-like mode of $In_{1-x}Ga_xAs$ is observable at 269 cm^{-1}. It appears that an additional peak is present at 265 cm^{-1}, which can be associated with GaAs-like mode of quartenary material or the GaAs-like mode of $In_{1-x}Ga_xAs$ with a slight indium enhancement. The intensity in the spectral region between 320 and 340 cm^{-1} is assigned to the InP-like modes of $InAs_xP_{1-x}$ or $In_{1-x}Ga_xAs_yP_{1-y}$. The InAs region (220 to 240 cm^{-1}) is dominated by the broad peak at 234 cm^{-1}, which we associate with the InAs-like LO mode of $In_{1-x}Ga_xAs$. The modes of InAs (bulk), strained InAs and the InAs-like mode of $In_{1-x}Ga_xAs_yP_{1-y}$ are also located in this region. This probably gives rise to the broad structure, from which it is very difficult (if not impossible) to obtain information on the interfaces.

Generally, in all Raman spectra of the CBE samples we observe a broad structure between 265 cm^{-1} and 270 cm^{-1}. In the Raman spectra of some older samples [24] this broadening did not occur, as shown in Figure 6.8. Nevertheless, there were also samples for which the same broadening in the spectra is present, as in the Raman spectra in this report. The only resemblance between these older samples and the samples in this work, is the wide $In_{1-x}Ga_xAs$ well (5 nm), while the sample of the spectrum in Figure 6.8 has a thinner well (2 nm). This implies that there could be a small composition gradient present in the thicker wells, which does not appear in the thinner wells. Another argument reinforces this explanation, namely the one that another III/III ratio is used for thick and for thin wells, namely 0.68 and 0.73 respectively.

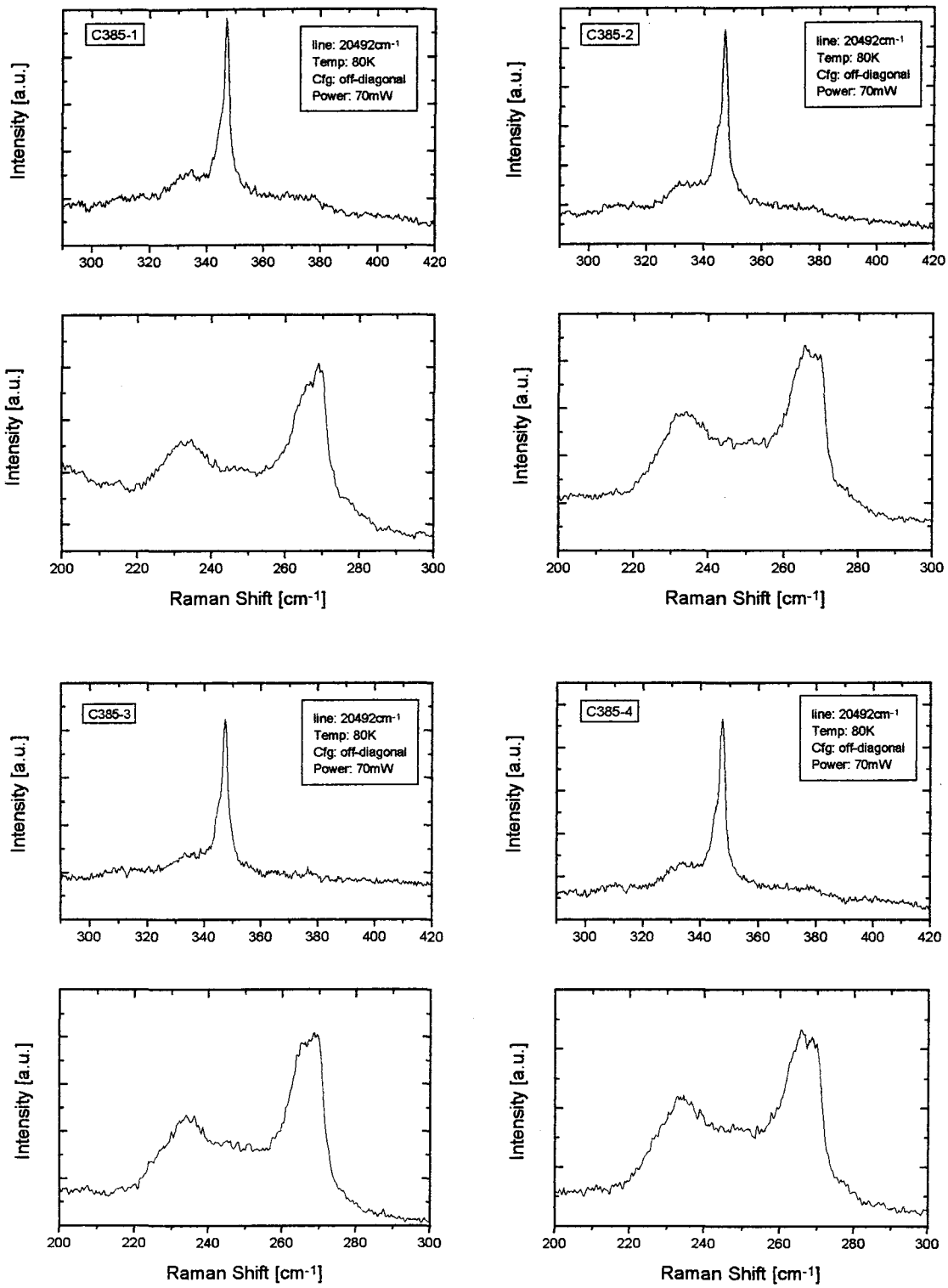

Figure 6.7: Raman spectra of samples with different misorientations, but with the same layer structure, i.e. GIS.

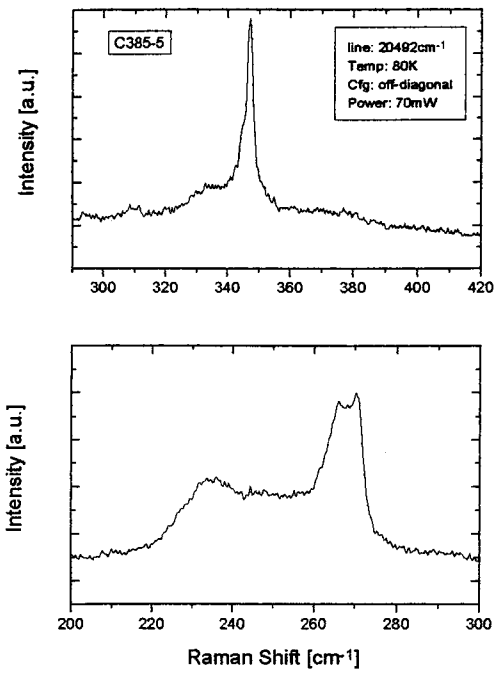

Figure 6.7 continued: see preceding page.

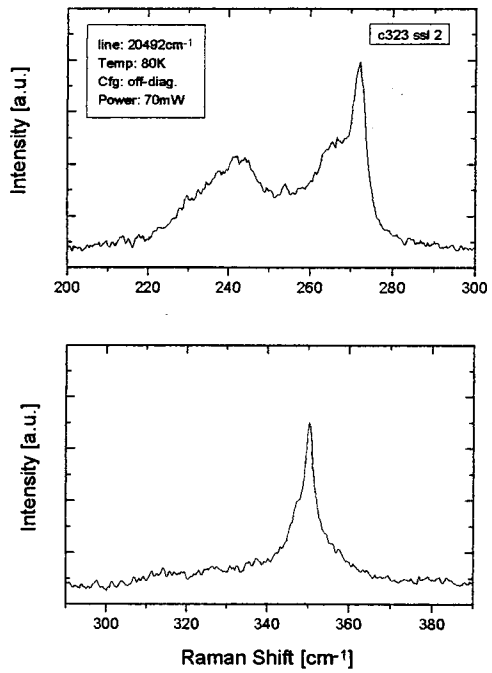

Figure 6.8: Raman spectrum of an $In_{1-x}Ga_xAs$ / InP sample with small wells (2 nm), instead of thick wells (5 nm).

7. Conclusions

Generally, we conclude that Raman spectroscopy is not suitable (or sensitive enough) for identification of interface layers. Hence, it is certainly not sensitive enough to obtain significant additional information on the differences between the interfaces.

For the MBE samples we conclude that Raman spectroscopy does give little or no additional information on the interface layers. The InAs region is dominated by the InAs-like mode of the bulk $In_{1-x}Al_xAs$ and thus prevents us from resolving the broad structure around 246 cm^{-1}, which we associated with strained InAs at the interface. A compositional effect can be detected for the position of the InAs-like and the AlAs-like LO peaks.

In the Raman spectra of the CBE samples consisting of the InAs / InP superlattice, no intensity is observed in the InAs region (around 235 cm^{-1}). The samples with 0° and 0.5° misorientation show a surface mode in the corresponding Raman spectra. Furthermore, two additional peaks are observed at 305 cm^{-1} and 310 cm^{-1}, which belong either to the InP TO or to an IFM of $InAs_xP_{1-x}$. An unambiguous identification is not possible based on the measurements presented in section 6.2. An additional intensity can be concluded in the spectral region between 330 and 340 cm^{-1}. It is associated with the InP-like modes of the ternary $InAs_xP_{1-x}$. This would be consistent with the occurrence of $InAs_xP_{1-x}$ interface phonons.

The Raman spectra of the different $In_{1-x}Ga_xAs$ / InP superlattices do not show significant structural differences. Hence little or no extra information on the interfaces or layer structure is obtained. The origin of the broadening of the GaAs-like mode associated with $In_{1-x}Ga_xAs$ is either a slight indium enhancement in the layer or a quartenary GaAs-like mode. No obvious distinction can be made based on the Raman measurements presented in this work. Comparison with older Raman spectra indicates that the broad structure around 265-270 cm^{-1} can also be due to a indium gradient in the $In_{1-x}Ga_xAs$ layer.

8. Suggestions

We divide the suggestions in two parts, namely a part concerning further Raman investigations and a part concerning other techniques. We start with the first part.

In order to resolve the structure in the InAs region (of the Raman spectra) due to interface layers, resonant Raman measurements on InAs can be performed for both MBE and CBE samples. For that purpose a tuneable laser is required which enables an exact match of the light energy with an electronic transition energy in the InAs.

When we want to decompose the structures in the spectra of $In_{1-x}Ga_xAs$ / InP superlattices, we need more simple samples as a basis for further interpretation. For example, bulk InP or lattice matched bulk $In_{1-x}Ga_xAs$ on InP substrates with various misorientations. In order to explain the peaks around 350 cm^{-1} and 310 cm^{-1} in the InAs / InP superlattices, we need more Raman measurements on different samples with various misorientations.

For MBE, more samples are needed in order to continue the investigation on the InAs interface layer formation. The samples have to be grown at even more distinct growth parameters such as the annealing time, As_2/As_4 use, growth temperature etc. Information on the mechanism of the InAs island formation, could be obtained from photoluminescence spectroscopy [13]. Furthermore, we propose to perform photoluminescence excitation (PLE) measurements on both MBE and CBE samples, in order to determinate the exact energy of the electronic transitions. Photoluminescence (PL) does not give this information, since the Stokes shift is involved. Finally, we can try to perform Scanning-Tunnel-Microscopy (STM) measurements on the cleaved side of the MBE samples. This can give important information on the structure and the dimensions of the islands.

References

[1] Chris G. van de Walle, Phys. Rev. B 39, 1871 (1989-II).
[2] J.W. Matthews and A.E. Blakeslee, J. Cryst. Growth. 27, 118 (1974).
[3] R.T.H. Rongen et al, J.Cryst. Growth. 164, 263 (1996).
[4] Dissertation, T. Marschner, Universität Marburg, (1995).
[5] Semiconductors & Semimetals, vol. 22 part A, W.T. Tsang, AT&T Bell Labs, chapter 2, p95.
[6] J.M. Moison, M. Benoussan and F. Houzay, Phys. Rev. B 34, 2018 (1986).
[7] G. Hollinger, D. Gallet, M. Gendry, C. Santenilli and P. Voktorovich, J. Vac. Sci. Technol. B 8, 832 (1990).
[8] R. Shioda, H. Oyanagi et al, Jpn. J. Appl. Phys. 33, 5623 (1994).
[9] R.T.H. Rongen et al, J. Cryst. Growth 164, 263 (1996).
[10] D. Vignaud, X. Wallert and F. Mollot, J. Appl. Phys. 76, 2324 (1994).
[11] A. Gustafsson, D. Hessman et al, J. Cryst. Growth 147, 27 (1995).
[12] B.X. Yang, L. He and H. Hasegawa, J. Electron. Mat. 25 , 379 (1996).
[13] Stageverslag H. Boom, Group Semiconductor Physics, Technical University Eindhoven, (1996).
[14] Vibrational Spectroscopy of Solids, P.M.A. Sherwood, Camebridge, University Press, (1972).
[15] The Physics of Phonons, G.P. Srivastava, University of Exeter, IOP Publishing Ltd, (1990).
[16] Solid State Physics and Applications, R.J. Elliot and A.F. Gibson, Oxford /Essex, (1974).
[17] I.F. Chang and S.S. Mitra, Phys. Rev. 172 , 924 (1968).
[18] J. Hermans, Diplomarbeit, I. Physikalisches Institut, RWTH Aachen, (1991).
[19] J. Geurts and N. Esser, Raman spectroscopy in: Optical characterization of Epitaxial Semiconductor Layers; Eds: G. Bauer and W. Richter, Springer, Heidelberg (1996).
[20] Scattering of Light by Crystals, W. Hayes and R. Loudon, John Wiley and sons Inc. (1978).
[21] Group Theory and Quantum Mechanics, M. Tinkham, (1964).

[22] M. Cardona in "Topics in Applied Physics", Light Scattering in Solids II, vol. 50, ed. by M. Cardona and G. Güntherodt, Springer Verlag, (1982).
[23] H. Fröhlich, Adv. Physics 3, 325, (1954).
[24] M. Pohlmann, Diplomarbeit, I. Physikalisches Institut, RWTH Aachen, (1995).
[25] J. Tümmler, Diplomarbeit, I. Physikalisches Institut, RWTH Aachen, (1996).
[26] Landolt Börnstein, Numerical Data and Functional Relationships in Science and Technology III, new series vol. 22a, Springer Verlag, (1987).
[27] L. Pavesi, R. Houdré and P. Gianzozzi, J. Appl. Physics. 78 , 470 (1995).
[28] L.G. Quagliano, B. Jusserand and D. Orani, Solid State Elec. 40, 711 (1996).
[29] Shuichi Emura et al, Phys. Rev. B 38, 3280 (1988).
[30] B. Jusserand and S. Slempkens, Solid State Communications 49, 95 (1984).
[31] Dissertation, R.T.H. Rongen, Technical University Eindhoven, to be published (1996).
[32] Dissertation, J.M. Finders, RWTH Aachen (D82), (1992).

Acknowledgements

The work presented in this report would not have been possible without the fruitful contribution of many people. First of all, I would like to thank Ir. C.M. van Es and dipl.-phys. R.T.H. Rongen for their guidance during my trainee period at the Technical University in Eindhoven (TUE). Their help and inspiring discussions have helped me a lot and kept me on the right track.

Then I thank Prof. dr. J. Geurts (currently in Würzburg) for giving me the opportunity to perform Raman measurements at the Rheinisch-Westfälischen Technischen Hochschule (RWTH) in Aachen and for the interesting discussions we had. My gratitude goes to dipl.-phys. J. Tümmler, for making me acquainted with the Raman set-up and for the nice time we had together in Aachen.

Furthermore, Dr. ir. F.A.P. Blom and Prof. dr. J.H. Wolter are acknowledged for making this project possible and for the smooth administrative guidance.

Finally, I would like to thank all members of the Semiconductor Group at the TUE and the RWTH Aachen for making my period in these groups a very pleasant and unforgettable one.